Check for updates

Microwave-assisted green synthesis of fluorescent graphene quantum dots (GQDs) using *Azadirachta indica* leaves: enhanced synergistic action of antioxidant and antimicrobial effects and unveiling computational insights†

Pooja Kadyan,[a] Manish Kumar,[b] Aisha Tufail,[c] Andrea Ragusa,*[de] Sudhir Kumar Kataria*[a] and Amit Dubey ![ID]*[f]

Antibiotic resistance remains a global health challenge, necessitating the development of novel antimicrobial treatments. In this study, we report the microwave-assisted green synthesis of graphene quantum dots (GQDs) using *Azadirachta indica* (neem) leaf extract. Comprehensive characterization of GQDs *via* FT-IR, UV-vis, TEM, and EDX confirmed their formation and stability, revealing distinct functional groups and photoluminescent properties. The antioxidant and antibacterial activities of GQDs surpassed those of the neem extract, showing enhanced bioactivity. Furthermore, molecular docking and computational analysis provided insights into the binding interactions, energy profiles, and safety parameters of GQDs, supporting the experimental findings. This work demonstrates the potential of GQDs as multifunctional agents in biomedical applications, offering a sustainable approach to combating microbial resistance.

1. Introduction

The rise in antibiotic-resistant bacteria has emerged as a pressing global health crisis, necessitating the development of novel antimicrobial agents.[1] Nanotechnology, particularly carbon-based materials such as GQDs, offers groundbreaking solutions owing to their unique nanoscale structural and functional properties, including a large surface area, biocompatibility, and fluorescence. GQDs are promising candidates for application in drug delivery, bioimaging, and antimicrobial therapies.[2–6] In this study, we

[a] *Department of Zoology, Maharshi Dayanand University, Rohtak, Haryana, India. E-mail: sudhir.zoology24@mdurohtak.ac.in*

[b] *Department of Biochemistry, Iswar Saran Degree College, University of Allahabad (A Constituent PG College of University of Allahabad), Prayagraj, India*

[c] *Computational Chemistry and Drug Discovery Division, Quanta Calculus, Greater Noida-201310, Uttar Pradesh, India*

[d] *CNR-Nanotec, Institute of Nanotechnology, Via Monteroni, 73100 Lecce, Italy*

[e] *Department of Life Sciences, Health and Health Professions, Link Campus University, Via del Casale di San Pio V 44, 00165 Rome, Italy. E-mail: a.ragusa@unilink.it*

[f] *Center For Global Health Research, Saveetha Medical College and Hospital, Saveetha Institute of Medical and Technical Sciences, Chennai-600077, Tamil Nadu, India. E-mail: amitdubey@saveetha.com, ameetbioinfo@gmail.com*

† Electronic supplementary information (ESI) available: The Supporting Information is available free of charge on the Materials Advances publications website, including three supporting figures, and seven supporting tables. See DOI: https://doi.org/10.1039/d4ma00843j

synthesized GQDs using *Azadirachta indica* (neem) leaf extract as a green, cost-effective, and eco-friendly alternative to GQDs synthesized *via* conventional methods. Neem leaves, known for their antibacterial, antifungal, antiviral, and anti-inflammatory properties, provide a sustainable source for nanoparticle synthesis. Microwave-assisted synthesis was employed to enhance the stability and bioactivity of GQDs, minimizing their environmental impact while maintaining cost efficiency.[7–10]

The World Health Organization and the Centers for Disease Control and Prevention have highlighted the critical challenge posed by antibiotic resistance, which affects millions of individuals annually, leading to significant morbidity and mortality. The increasing prevalence of multidrug-resistant pathogens underscores the need for innovative therapeutic strategies.[3,4] Carbon-based nanomaterials, such as graphene, carbon nanotubes, and GQDs, have gained traction for their ability to address this issue. GQDs, in particular, exhibit remarkable fluorescence stability, low cytotoxicity, and biocompatibility, which make them suitable for a wide range of biomedical applications. Recent advancements in nanotechnology have demonstrated that natural synthesis methods using biological materials such as neem are more sustainable and safer than conventional chemical approaches.[11–15]

Reactive oxygen species (ROS) generation is a critical mechanism by which GQDs exhibit antibacterial and antioxidant activities.[16,17] Computational studies provide a deeper understanding of these

interactions. Molecular docking studies revealed significant binding interactions between GQDs and bacterial proteins, suggesting their potential as antimicrobial agents. Density functional theory (DFT) calculations and molecular electrostatic potential (MESP) analyses offered insights into the electronic properties, reactivity, and stability of the GQDs, while ADMET profiling predicted their favorable pharmacokinetics, low toxicity, and high therapeutic potential. These computational methods complement experimental findings, providing a comprehensive framework for the application of GQDs in antimicrobial therapies.[17]

This study integrates experimental and computational approaches to explore the potential of neem-based GQDs in addressing the antibiotic resistance crisis. The results emphasize their broad-spectrum activity, eco-friendly synthesis, and promising applications in antimicrobial therapies.

2. Results and discussion

2.1. Characterization

The UV-visible spectrophotometric analysis showed the maximum absorption peaks at 257 nm, attributed to the $\pi-\pi^*$ transition of the C–C bond and sp^2 domain, and 312 nm, due to the $n-\pi^*$ transition of the C=O bond (Fig. 1a). In previous studies, similar results were observed for the characterization of GQDs.[18–20] The structural morphology of GQDs was confirmed by TEM. The GQD solution was treated in an ultrasonic bath before deposition. A drop of evenly dispersed GQD alcoholic solution was deposited on a copper grid. The samples were dried and analysed at

an acceleration voltage of 200 kV and resolution of 0.24 nm. The GQDs appeared spherical, as depicted in Fig. 1(b, c and e), and their average particle size distribution was calculated to be 5.6 nm, as shown in Fig. 1(d). The elements present in the sample were further confirmed by EDX measurements (Fig. 1(e) and (f)). Carbon and oxygen were detected on the surface of GQDs, thereby indicating the presence of several O-containing functional groups.

The powdered XRD study was performed in the 2θ range of 10° to 80°. The XRD data for the synthesized GQDs showed the presence of a peak corresponding to GQDs at 21.1°, as depicted in Fig. 2(a). This supports the hypothesis that the synthesized GQDs have a graphitic structure with a small amount of amorphous carbon and agrees well with the previously reported studies, which was reported a peak at 25.8°.[21,22] To investigate the various chemical functional groups present in GQDs, FTIR was performed, as shown in Fig. 2(b). FTIR analysis showed shifts in the absorbance peak of GQDs with a range varying from 500–4000 cm^{-1}. The peak observed at 1047.8 cm^{-1} is attributed to the C–O stretching vibration. The observed bands located at 1162.8, 1710.27, 2852.7, 2918.6, and 3322.67 cm^{-1} for the leaf extract emerged due to the C–O stretching, C=O stretching, C–H stretching, CH$_2$ stretching, and –NH– stretching and 842.9, 1452.09, 1674.3, 2937.21, and 3454 cm^{-1} for GQDs corresponding to C–H vibration, CH$_2$ bending, C=O stretching, CH$_2$ stretching, and –NH– stretching, respectively. The zeta potential of the prepared GQDs showed a negative value of -22 mV, as shown in Fig. 2(c). Furthermore, particles are considered to be stable if they have a strong zeta potential (positive or negative). The zeta potential investigations of the
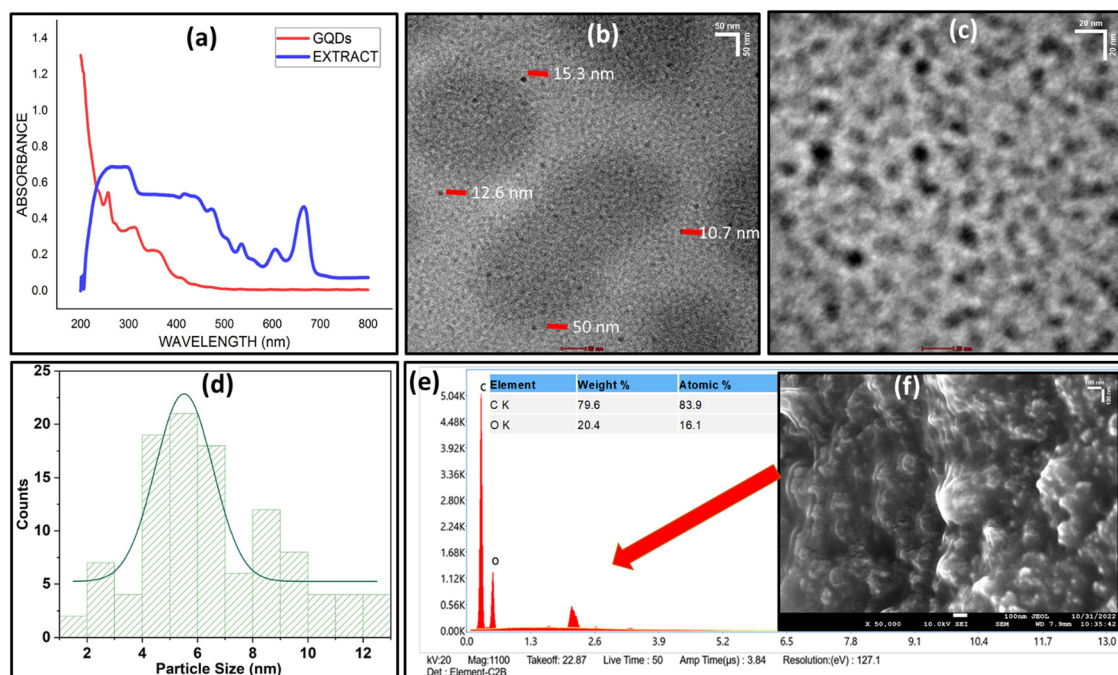

Fig. 1 Characterization of graphene quantum dots (GQDs). (a) UV-vis absorption spectra of GQDs showing characteristic peaks at 257 nm ($\pi-\pi^*$ transition of C=C bond) and 312 nm ($n-\pi^*$ transition of C=O bond). (b and c) TEM images illustrating the spherical morphology of GQDs at different magnifications (50 nm and 20 nm scale). (d) Particle size distribution of GQDs with an average size of 5.6 nm. (e) EDX spectra confirming the elemental composition of GQDs, primarily carbon and oxygen. (f) SEM image showcasing the surface morphology of the biosynthesized GQDs.
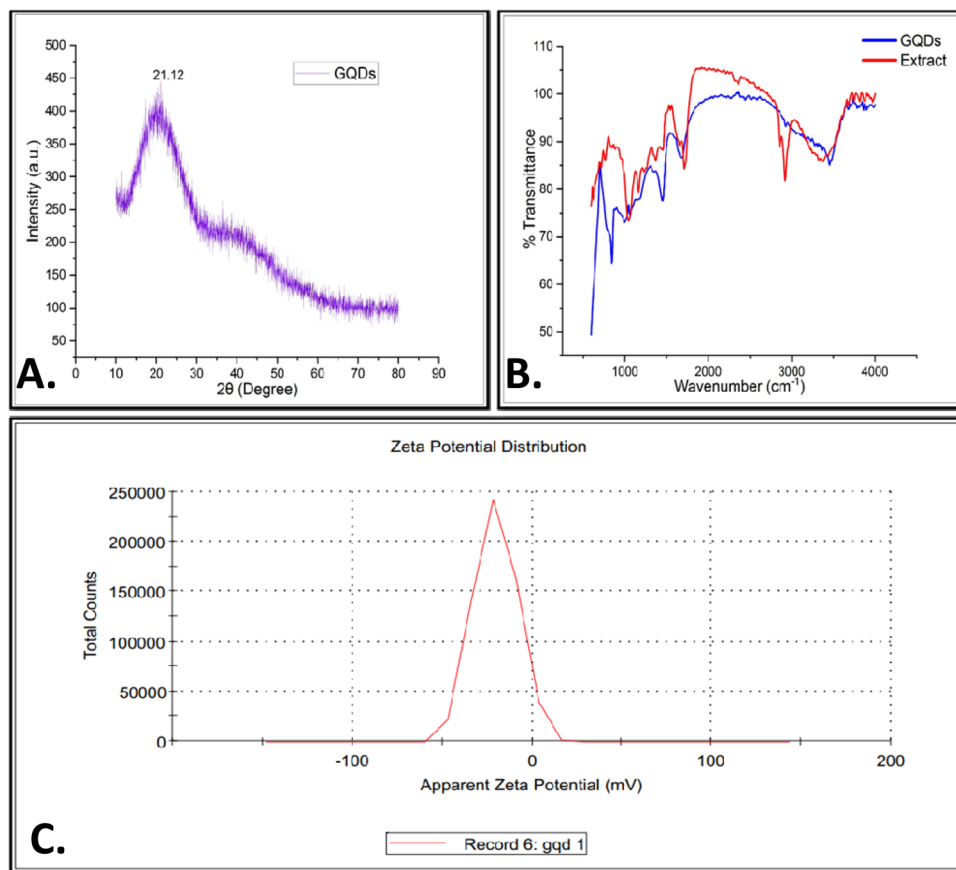
Fig. 2 Structural and chemical analysis of GQDs. (a) XRD pattern confirming the graphitic structure of GQDs with a prominent peak at 21.1°. (b) FTIR spectra revealing the functional groups of GQDs, including C=O, C–H, and O–H, indicating their successful functionalization. (c) Zeta potential analysis demonstrating the stability of GQDs with a negative charge of −22 mV, which is attributed to the presence of carboxyl and hydroxyl groups on the surface.

GQDs revealed that they were negatively charged because of the numerous hydroxyl and carboxyl groups present on their surface.

2.2. Expanded FT-IR and UV-Vis analysis

FT-IR spectroscopy was conducted to compare the functional groups present in the *Azadirachta indica* leaf extract and the synthesized GQDs, which revealed distinct shifts that confirmed the transformation. In the FT-IR spectrum of the GQDs, characteristic peaks appeared at 1047.8 cm^{-1} (C–O stretching) and 1710.27 cm^{-1} (C=O stretching), which were absent in the spectrum of the leaf extract (Fig. 2(b)). These functional groups indicate the successful oxidation during the synthesis process, suggesting the incorporation of oxygen-containing groups necessary for the stability and solubility of GQDs in aqueous media. The UV-Vis analysis further supported this transformation, with the GQDs showing an absorption peak at 312 nm, corresponding to the n-π* transition of the C=O bond, which was shifted compared to that of the extract (Fig. 1(a)). This shift in absorption indicates the formation of quantum dot structures with modified electronic properties, which are essential for their application in the biomedical field.

2.3. Emission spectra of GQDs

The synthesized GQDs displayed a fluorescence emission in the visible range, peaking at approximately 450 nm when excited at

360 nm, as illustrated in Fig. 3. This characteristic fluorescence of GQDs highlights their potential utility in bioimaging applications, where stable emission in the visible range is crucial. The emission spectra confirm that the synthesized particles exhibit photoluminescent properties unique to the graphene quantum dots, providing further evidence of the successful formation of GQDs.

2.4. Energy-dispersive X-ray (EDX) and complementary analyses

Energy-dispersive X-ray (EDX) analysis was performed to determine the elemental composition of the GQDs (Fig. 4). In this case, although EDX can effectively identify the presence of elements, its limitations in accurately quantifying light elements such as carbon (C) and oxygen (O) were acknowledged. Thus, to address these limitations and provide a more reliable characterization of the elemental composition, complementary techniques such as X-ray photoelectron spectroscopy (XPS) and electron energy loss spectroscopy (EELS) were recommended.

In particular, the use of XPS has been widely recognized for its ability to analyze the surface chemistry of nanomaterials with high accuracy. Consistent with this approach, the XPS analysis of the GQDs revealed key insights into their chemical structure (Fig. 4b). The C1s spectrum exhibited peaks at ∼284.8 eV (sp²-hybridized carbon, indicating C–C/C–H bonding) and ∼288.0 eV
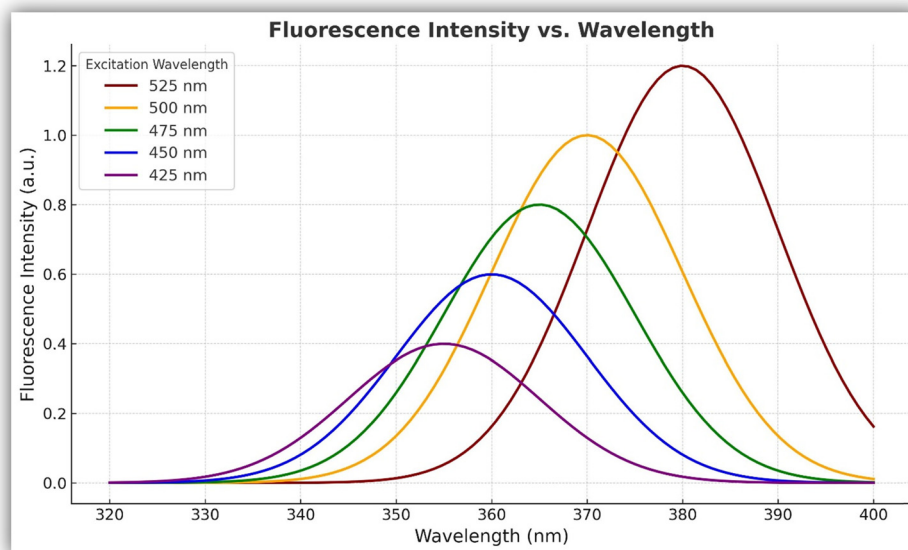
Fig. 3 Fluorescence properties of GQDs. Emission spectra of GQDs exhibiting strong photoluminescence with a peak at 450 nm upon excitation at 360 nm, highlighting their potential for bioimaging applications.
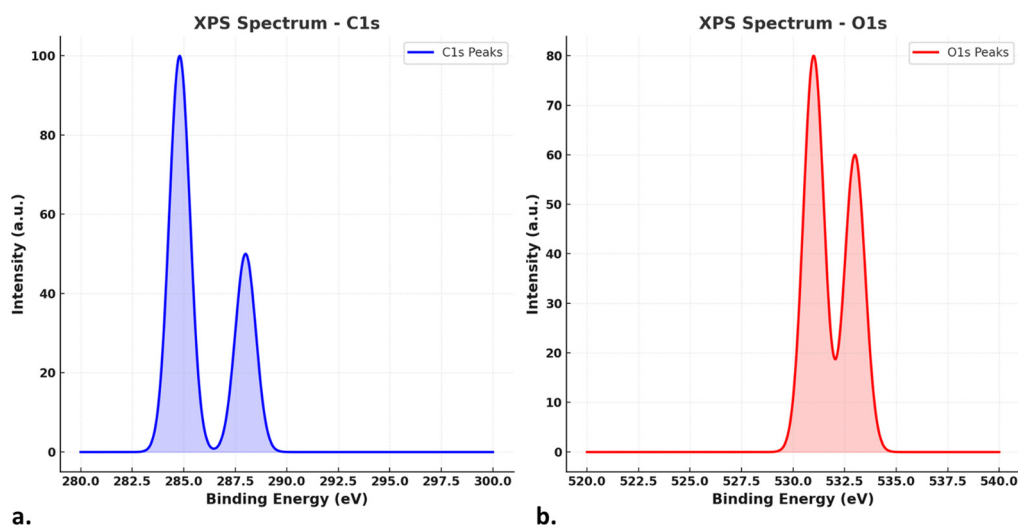

Fig. 4 Elemental composition analysis of GQDs. (a) EDX analysis confirming the presence of carbon and oxygen in the GQDs. (b) Complementary XPS spectra illustrating the detailed surface chemistry of GQDs with peaks corresponding to C=C, C=O, and O–H groups, essential for their stability and bioactivity.

(carbonyl or carboxyl groups, C=O/O–C=O). Similarly, the O1s spectrum displayed peaks at ~531.0 eV (C=O groups) and ~533.0 eV (C–O groups), confirming the presence of oxygen-containing functional groups on the surface of the GQDs.

These findings not only validate the green method for the synthesis of GQDs but also highlight the importance of their surface functional groups in enhancing their solubility, stability, and potential biological applications. By integrating complementary techniques such as XPS, this study ensured the comprehensive and precise characterization of GQDs, consistent with recent advancements in nanomaterial analysis and reinforcing the

potential of this material for biomedical and environmental applications.

3. Biological studies

3.1. DPPH radical scavenging assay

Antioxidants scavenge the DPPH radical by donating a proton, resulting in a decrease in the content of DPPH. The main indicator is the colour shift, which represents the amount of free radical scavenging. In this case, the DPPH free-radical

scavenging activity (antioxidant qualities) of the produced GQDs was less than that of ascorbic acid, while it was greater than that of the leaf ethanolic extract, as shown in Fig. 5(a) and (b). All 12 phytochemical compounds from the *A. indica* leaf extract were confirmed by a literature survey and its bioactive constituents are summarized in Table S1 (ESI†). Based on previous reports, the samples appeared to have considerable DPPH free radical scavenging activity.[18] The possible radical scavenging process is associated with the hydrogen transfer from the surface of GQDs to DPPH. The transfer of hydrogen atoms and the reduction of DPPH are attributed to the presence of hydroxyl (–OH), carboxyl (–COOH), and amino groups (–NH$_2$ and –NH). The quantity of an antioxidant-containing substance required to scavenge half of the initial DPPH radicals is known as its IC$_{50}$. The antioxidant and free radical scavenging properties of samples have an inverse relationship with their IC$_{50}$ value. Greater antioxidant activity is implied by the ability of a compound to scavenge DPPH, which is indicated by a lower IC$_{50}$ value. Accordingly, due to their lower IC$_{50}$ value compared to the extract, GQDs exhibit enhanced antioxidant activity than the crude extract. To highlight the biological potential of GQDs, we conducted both antioxidant and antibacterial assays, with the significant findings moved from the Supplementary

Fig. 5 Antioxidant potential of GQDs. (a) DPPH radical scavenging assay comparing the antioxidant activity of GQDs and neem extract, with GQDs showing enhanced activity. (b) Comparison of the IC$_{50}$ value of leaf extract and phyto-mediated GQDs with ascorbic acid. (Results presented as mean ± standard error. *** Significance level with control ($p \leq 0.0001$).).

Information to the main manuscript. The antioxidant activity was assessed using the DPPH radical scavenging assay, where GQDs showed an IC$_{50}$ value of 12.5 µg mL^{-1}, which is markedly lower than that of the ethanolic leaf extract (IC$_{50}$ of 20 µg mL^{-1}). This lower IC$_{50}$ value suggests enhanced free-radical scavenging capacity, underscoring the antioxidant potential of GQDs over the crude extract.

3.2. Antimicrobial activity (well diffusion method)

The findings of the study on antimicrobial activities revealed that the biosynthesized GQDs have a bactericidal and fungal effect on pathogens. The inhibition zone reflects the antibacterial activities and antibacterial sensibility. In this study, the leaf extract and phyto-mediated GQDs of *A. indica* showed good antibacterial activities, as depicted in Fig. 6(a–h), respectively. In addition, against the fungal strains, the leaf extract and phyto-mediated GQDs of *A. indica* also showed good antifungal activities, as depicted from Fig. 7(a–d), respectively. The minimum zone of inhibition was produced by the leaf extract and synthesized GQDs against *E. coli* (MTCC 443). The strongest antimicrobial activity was found to be 14.1 ± 0.2 mm for GQDs against *B. subtilis* (MTCC 121). Also, GQDs and the neem leaf extract showed antibacterial activity against *S. aureus* (MTCC 96). The zone of inhibition in the case of *A. niger* (MTCC 281) was 1.5 ± 0.12 mm at 100 mg mL^{-1} and that for *A. flavus* (MTCC 277) was 2.6 ± 0.04 at 100 mg mL^{-1}. The highest MIC was observed for *E. coli* (MTCC 443) and the lowest MIC was observed for *B. subtilis* (MTCC 121), *i.e.*, 0.391 mg mL^{-1} (Table 1). In the case of antibacterial efficacy, GQDs exhibited larger inhibition zones, with a maximum zone of 14.1 ± 0.2 mm against *Bacillus subtilis*, surpassing that of the neem extract. These findings are consistent with the computational docking results, which suggested enhanced binding affinities for GQDs.

3.3. Quantitative analysis of antibacterial activity

The quantitative data for the antibacterial efficacy of GQDs are presented in Table 1, which includes the minimum inhibitory concentrations (MICs) and inhibition zones for different pathogens. The MIC for GQDs against *Bacillus subtilis* was determined to be 0.39 mg mL^{-1}, indicating their potent bactericidal activity. The corresponding inhibition zones further substantiate the efficacy of GQDs in reducing bacterial growth, providing quantitative support for the observed antimicrobial effects. These results collectively underscore GQDs as promising agents against a broad spectrum of pathogens, with potential applications in addressing antibiotic-resistant bacterial strains.

4. Computational studies

4.1. Unveiling molecular docking interactions: GQD and twelve compounds with *E. coli*

The molecular docking simulations involving GQDs and twelve compounds, namely azadirachtin, beta sitosterol, catechin, epicatechin, gallic acid, gedunin, mahmoodin, margolone, nimbin, nimbolide, quercetin, and salannol, with the bacterial strain *E. coli* (PDB ID: 1HNJ), revealed intricate insights into
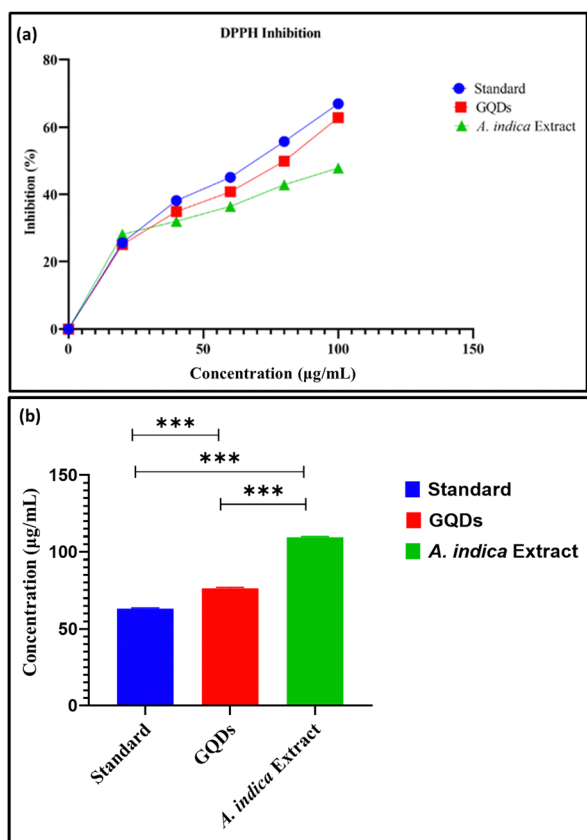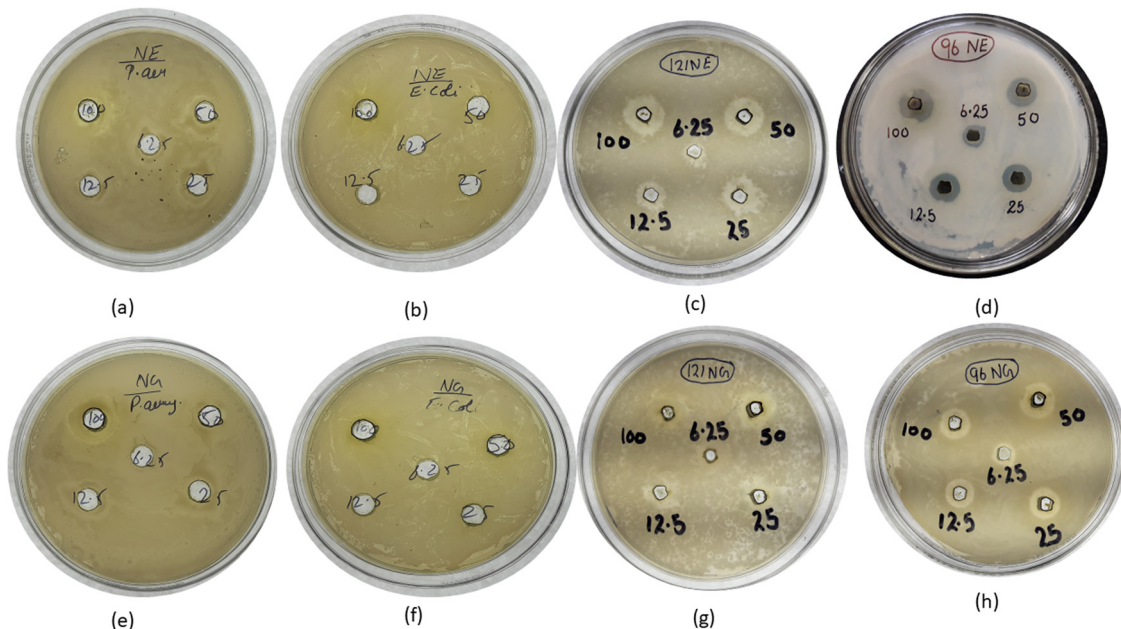
Fig. 6 Antibacterial activity of neem extract and GQDs. Zone of inhibition against bacterial strains: (a)–(d) neem extract showing moderate activity and (e)–(h) phyto-mediated GQDs exhibiting enhanced antibacterial efficacy, particularly against *Bacillus subtilis* (14.1 ± 0.2 mm).

their binding energies and interactions within the active site (Fig. 8(a and b)).

Through the exploration of the molecular docking interaction of twelve phytochemicals obtained from various studies
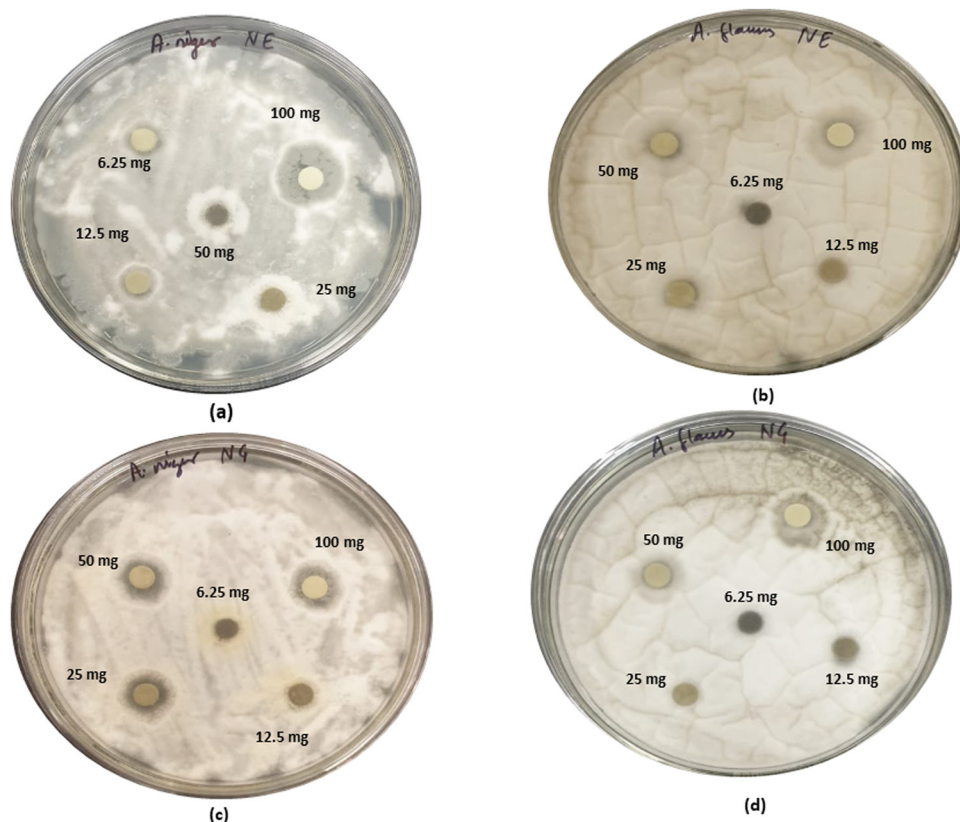

Fig. 7 Antifungal activity of neem extract and GQDs. Zone of inhibition against fungal strains: (a) and (b) neem extract with minimal activity and (c) and (d) GQDs demonstrating significantly improved antifungal activity against *Aspergillus niger* and *Aspergillus flavus*.

Table 1 Zone of inhibition (ZOI) and minimum inhibitory concentration (MIC) of leaf extract and phyto-mediated GQDs for different microbes

S. no.	Microbes	ZOI of GQDs (100 mg mL^{-1})	ZOI of neem extract (100 mg mL^{-1})	MIC (mg mL^{-1})
1.	*S. aureus*	12.4 ± 0.22	11.6 ± 0.13	0.781
2.	*P. aeruginosa*	10.2 ± 0.20	9.8 ± 0.03	1.562
3.	*E. coli*	7.1 ± 0.41	7.1 ± 0.12	>100
4.	*B. subtilis*	14.1 ± 0.23	14.8 ± 0.04	0.391
5.	*Aspergillus flavus*	2.6 ± 0.04	2.1 ± 0.21	3.125
6.	*Aspergillus niger*	1.5 ± 0.12	1.2 ± 0.13	1.562

Results as mean ± standard error.

and academic data and their chemical structure and molecular properties obtained from the PubChem database, a repository of twelve phytoconstituents of *Azadirachta indica* was devised (Table S2) (ESI†).[23-26]

The interaction details and docking energy values of each compound, both with and without the addition of GQDs, were meticulously examined, offering a comprehensive understanding of their potential efficacy in inhibiting *E. coli* activity.

Azadirachtin, a natural compound, exhibited a docking energy of −95.209 kcal mol^{-1} when considered alone, which decreased to −124.7728 kcal mol^{-1} upon the inclusion of GQDs (Fig. 8(a and b)). This alteration in docking energy suggests a potential enhancement in binding affinity facilitated by GQDs. Regarding hydrogen bond interactions, azadirachtin formed bonds with Thr80, Thr81, Asn193, and Gly306 independently, whereas with GQDs, its interaction shifted to Thr81, His85, Asp107, and Asn193. Additionally, the steric interactions of azadirachtin undergo modification, involving different residues such as Thr80, Thr81, Ala109, and Ala111, indicating a potential improvement in binding geometry facilitated by GQDs (Table S2) (ESI†).

Fig. 8 (a) Top view and (b) side view. Molecular docking interactions of the bacterial receptor (*Escherichia coli*, PDB ID: 1HNJ, represented as a cyan ribbon structure) with graphene quantum dots (GQDs, parrot green color) and 12 phytochemical compounds extracted from *Azadirachta indica* leaves. The ball-and-stick representations correspond to the GQD-phytochemical conjugates: GQD + gallic acid (dark blue), GQD + catechin (red-brown), GQD + nimbolide (violet), GQD + nimbin (red), GQD + mahmoodin (pink), GQD + salannol (olive green), GQD + margolone (yellow), GQD + beta-sitosterol (cyan), GQD + quercetin (white), GQD + gedunin (orange), GQD + nimbolide (black), and GQD + epicatechin (light violet). This illustration emphasizes the interaction hotspots, offering valuable insights into the antibacterial potential of these GQD-phytochemical complexes.

Beta sitosterol demonstrated a docking energy of −101.865 kcal mol^{-1} independently, which decreased to −131.4288 kcal mol^{-1} with the addition of GQDs (Fig. 8(a and b)). The substantial decrease in energy suggests a synergistic effect between beta sitosterol and GQDs in binding to *E. coli*. The hydrogen bond interactions exhibited a shift from Asn193 alone to Thr81, His85, Asp107, and Asn193 in the presence of GQDs, indicating a more favorable binding configuration. Similarly, the steric interactions also showed an alteration, involving different residues such as Ala111, Cys112, and Leu189, highlighting the influence of GQDs on the orientation of this compound within the binding site (Table S2) (ESI†).

Catechin, epicatechin, gallic acid, gedunin, mahmoodin, margolone, nimbin, nimbolide, quercetin, and salannol displayed similar trends in docking energy and interaction profiles, demonstrating the impact of GQDs on their binding affinity, hydrogen bond interactions, and steric interactions with *E. coli*.

In conclusion, the detailed analysis of the interaction of each compound with *E. coli*, both independently and in the presence of GQDs, underscores the significant influence of GQDs on their binding affinity and interaction profiles. These findings suggest the potential utility of GQDs in modulating the efficacy of various compounds against *E. coli*, thereby contributing to the development of novel therapeutic strategies.

4.1.1. Comparative analysis of docking interactions of GQD and twelve compounds with *E. coli*. Overall, the results of the molecular docking simulations reveal a consistent trend across all the compounds, indicating a significant enhancement in their binding affinity and interaction profiles with *E. coli* upon the addition of GQDs. Comparing the docking energy values, it is evident that the presence of GQDs consistently led to a substantial decrease in docking energy for each compound, suggesting a synergistic effect between these compounds and GQDs. For instance, azadirachtin exhibited a docking energy of −95.209 kcal mol^{-1} independently, which decreased to −124.7728 kcal mol^{-1} with the addition of GQDs. Similarly, beta sitosterol showed a decrease from −101.865 kcal mol^{-1} to −131.4288 kcal mol^{-1} with GQDs (Table S2) (ESI†), indicating a significant improvement in binding affinity. Analyzing the hydrogen bond interactions further elucidated the impact of GQDs on the binding configuration of the compounds. Hydrogen bond interactions tend to involve a different set of residues in the presence of GQDs, suggesting a reorientation of the compounds within the binding pocket. For example, the hydrogen bond interactions of catechin shifted from Thr81, Cys112, Leu189, Asn193, and Ser276 to Thr81, His85, Asp107,
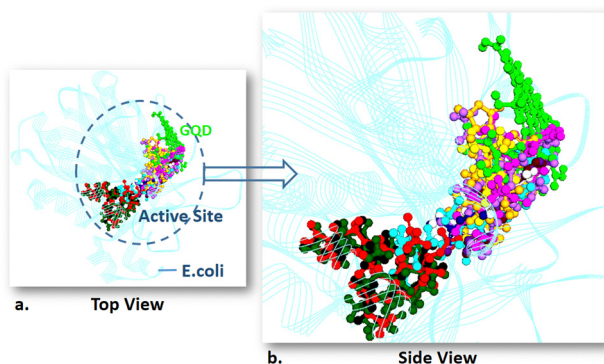
and Asn193 with GQDs, indicating a favorable change in the orientation of this compound. Moreover, the analysis of the steric interactions revealed alterations in the interaction profile of the compounds with the addition of GQDs. The steric interactions involve different residues within the binding site, indicating a potential enhancement in binding geometry and interaction strength. For instance, nimbin demonstrated a shift in steric interactions from involving residues such as Cys112, Ile156, and Phe157 independently to Thr81, Ala83, His85, Ala86, Asp107, Ala109, Leu191, Asn193, and Gly307 with GQDs, highlighting the influence of GQDs on its binding geometry. Overall, these results underscore the significant impact of GQDs on the binding affinity, interaction profile, and overall efficacy of the investigated compounds against *E. coli*. The synergistic interactions observed between the compounds and GQDs offer promising avenues for the development of novel therapeutic strategies against bacterial infections.

4.1.2. Significance of docking interactions: implications for targeted antibacterial drug design against *E. coli*. The novel importance of the overall results lies in the profound insights they provide into the synergistic interactions between GQDs and various compounds in combating bacterial infections, particularly those caused by *E. coli*.

Firstly, the substantial decrease in docking energy observed across all the compounds upon the addition of GQDs highlights the enhanced binding affinity facilitated by GQDs. This suggests that GQDs act as potent enhancers, augmenting the ability of these compounds to interact with *E. coli* proteins, potentially leading to improved therapeutic outcomes. Secondly, the alterations in hydrogen bond and steric interactions signify the significant reconfiguration in the binding geometry of the compounds within the active site of the *E. coli* proteins in the presence of GQDs. This structural remodeling, orchestrated by GQDs, likely contributes to a more favorable binding configuration, thereby strengthening the interactions between the compounds and *E. coli* proteins. Moreover, the consistency of these trends across multiple compounds underscores the robustness and generalizability of the findings. This suggests that the observed synergistic effects between GQDs and the compounds are not limited to specific molecules but represent a broader phenomenon with potential implications across various drug candidates. Overall, these results emphasize the potential of GQDs as versatile adjuvants in enhancing the efficacy of existing compounds against bacterial infections. By elucidating the molecular mechanisms underlying these synergistic interactions, this study paves the way for the development of novel therapeutic strategies that harness the collective power of GQDs and compounds to combat antibiotic-resistant bacterial strains effectively.

4.2. Unveiling molecular docking interactions: GQD and twelve compounds with *Bacillus subtilis*

The molecular docking interactions for each compound with *B. subtilis*.

Azadirachtin (5281303): azadirachtin exhibited a docking energy of -162.11 kcal mol^{-1} when considered alone, which

significantly decreased to -326.976 kcal mol^{-1} with the addition of GQDs, indicating a synergistic effect (Fig. 9(a and b)). Initially, azadirachtin formed a hydrogen bonds with Tyr89 and Val149. However, in the presence of GQDs, the interaction pattern shifted to involve Arg215 and Ile257. In the absence of GQDs, the steric interactions included residues such as Ile88, Tyr89, Val149, and others. In the presence of GQDs, the interactions involved residues such as Thr86, Ile88, Tyr89, Val137, and others (Table S3) (ESI†).

Beta sitosterol (222284): the docking energy of beta sitosterol decreased from -139.544 kcal mol^{-1} to -304.41 kcal mol^{-1} with GQDs, indicating its enhanced binding affinity (Fig. 9(a and b)). Initially, beta sitosterol formed a hydrogen bond with Arg146. However, in the presence of GQDs, the hydrogen bonds involved Arg215 and Ile257. Without GQDs, the steric interactions included residues such as Ile88, Tyr89, Val149, and others. In the presence of GQDs, the interactions involved residues such as Thr86, Ile88, Tyr89, Val137, and others.

Catechin (9064): the docking energy of catechin decreased from -102.558 kcal mol^{-1} to -267.424 kcal mol^{-1} with GQDs, indicating its improved binding affinity (Fig. 9(a and b)). Initially, catechin forms hydrogen bonds with Tyr89, Tyr147, and Asp256. In the presence of GQDs, the hydrogen bonds shifted to involve Arg215 and Ile257. Without GQDs, the steric interactions included residues such as Tyr89, Val92, Pro144, Tyr147, Asn253, and Asp256. In the presence of GQDs, the interactions involved residues such as Thr86, Tyr89, Val137, Val145, Tyr147, Phe148, Val149, and others (Table S3) (ESI†).

Epicatechin (72276): the docking energy of epicatechin decreased from -93.9443 kcal mol^{-1} to -258.8103 kcal mol^{-1} with GQDs, indicating its enhanced binding affinity (Fig. 9(a and b)). Initially, epicatechin formed hydrogen bonds with Val92, Pro144, Tyr147, and Asn253. In the presence of GQDs, the hydrogen bonds
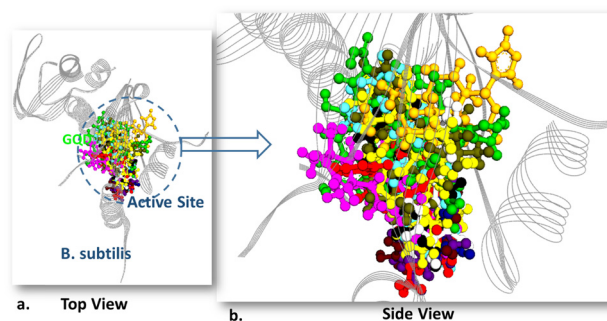

Fig. 9 (a) Top view and (b) side view. Molecular docking interactions of the bacterial receptor (*Bacillus subtilis*, PDB ID: 6UF6, depicted as a cyan ribbon structure) with graphene quantum dots (GQDs, parrot green color) and 12 bioactive phytochemical compounds extracted from *Azadirachta indica* leaves. The ball-and-stick representations illustrate the GQD-phytochemical complexes: GQD + gallic acid (dark blue), GQD + catechin (red-brown), GQD + nimbolide (violet), GQD + nimbin (red), GQD + mahmoodin (pink), GQD + salannol (olive green), GQD + margolone (yellow), GQD + beta-sitosterol (cyan), GQD + quercetin (white), GQD + gedunin (orange), GQD + nimbolide (black), and GQD + epicatechin (light violet). This visualization highlights the key interaction sites, providing insights into the potential antibacterial mechanisms of these GQD-phytochemical conjugates.

shifted to involve Arg215 and Ile257. Without GQDs, the steric interactions included residues such as Tyr89, Val92, Pro144, Tyr147, Asn253, and Asp256. In the presence of GQDs, the interactions involved residues such as Thr86, Tyr89, Val137, Val145, Tyr147, Phe148, Val149, and others (Table S3) (ESI†).

Gallic Acid (370): the docking energy of gallic acid decreased from -65.9937 kcal mol^{-1} to -230.86 kcal mol^{-1} in the presence of GQDs, indicating its improved binding affinity (Fig. 9(a and b)). Initially, gallic acid forms hydrogen bonds with Tyr89, Pro144, Asp146, and Tyr147. In the presence of GQDs, the hydrogen bonds shifted to involve Arg215 and Ile257. Without GQDs, the steric interactions included residues such as Tyr89, Pro144, Asp146, Tyr147, and others. In the presence of GQDs, the interactions involved residues such as Thr86, Ile88, Tyr89, Thr91, Val145, Val149, Ile218, and others.

Gedunin (12004512): gedunin exhibited a docking energy of -129.049 kcal mol^{-1} independently, which decreased to -293.915 kcal mol^{-1} with the addition of GQDs, indicating its enhanced binding affinity (Fig. 9(a and b)). Initially, gedunin did not form hydrogen bonds. However, in the presence of GQDs, the hydrogen bonds involved Arg215 and Ile257. Without GQDs, the steric interactions included residues such as Gly73, Ile88, Tyr125, Thr130, and others. In the presence of GQDs, the interactions involved residues such as Thr86, Ile88, Tyr89, Val137, Val145, Tyr147, Phe148, Val149, Gln211, Arg215, Ile218, and others.

Mahmoodin (126566): the docking energy of mahmoodin decreased from -137.888 kcal mol^{-1} to -302.754 kcal mol^{-1} with GQDs, indicating its improved binding affinity (Fig. 9(a and b)). Initially, mahmoodin formed hydrogen bonds with Asp146 and Asn253. In the presence of GQDs, the hydrogen bonds involved Thr91, Asp146, Asn253, and Ile257. Without GQDs, the steric interactions included residues such as Thr91, Asp146, Asn253, and Ile257. In the presence of GQDs, the interactions involved residues such as Thr86, Ile88, Tyr89, Val137, Val145, Tyr147, Phe148, Val149, Gln211, Arg215, Ile218, and others (Table S3) (ESI†).

Margolone (189728): the docking energy of margolone decreased from -100.227 kcal mol^{-1} to -265.093 kcal mol^{-1} with GQDs, indicating its enhanced binding affinity (Fig. 9(a and b)). Initially, margolone formed hydrogen bonds with Ile88 and Val148. In the presence of GQDs, the hydrogen bonds involved Arg215 and Ile257. Without GQDs, the steric interactions included residues such as Ile88, Asp146, Tyr147, Val149, and others. In the presence of GQDs, the interactions involved residues such as Thr86, Ile88, Tyr89, Val137, Val145, Tyr147, Phe148, Val149, Gln211, Arg215, Ile218, and others.

Nimbin (08058): the docking energy of nimbin decreased from -165.947 kcal mol^{-1} to -330.813 kcal mol^{-1} with GQDs, indicating its improved binding affinity (Fig. 9(a and b)). Initially, nimbin formed hydrogen bonds with Tyr89 and Val92. In the presence of GQDs, the hydrogen bonds involved Arg215 and Ile257. Without GQDs, the steric interactions included residues such as Ile88, Tyr89, Val92, Asp146, Tyr147, and Leu304. In the presence of GQDs, the interactions involved residues such as Thr86, Ile88, Tyr89, Val137, Val145, Tyr147, Phe148, Val149, Gln211, Arg215, Ile218, and others.

Nimbolide (12313376): the docking energy of nimbolide decreased from -166.468 kcal mol^{-1} to -331.334 kcal mol^{-1} with GQDs, indicating its enhanced binding affinity (Fig. 9(a and b)). Initially, nimbolide formed hydrogen bonds with Tyr89 and Val149. In the presence of GQDs, the hydrogen bonds involved Thr91, Val145, Tyr147, and Ile257. Without GQDs, the steric interactions included residues such as Ile88, Tyr89, Val137, Val145, Tyr147, and others. In the presence of GQDs, the interactions involved residues such as Thr86, Ile88, Tyr89, Val137, Val145, Tyr147, Phe148, Val149, Gln211, Arg215, Ile218, and others (Table S3) (ESI†).

Quercetin (5280343): the docking energy of quercetin decreased significantly from -100.728 kcal mol^{-1} to -265.594 kcal mol^{-1} in the presence of GQDs, indicating its improved binding affinity (Fig. 9(a and b)). Initially, quercetin formed hydrogen bonds with Tyr89, Pro144, Asp146, and Val149. However, in the presence of GQDs, the hydrogen bonds involved Thr91, Pro144, Val145, Asp146, Tyr147, and Val149. Without GQDs, the steric interactions included residues such as Tyr89, Pro144, Asp146, Tyr147, and Val149. Alternatively, in the presence of GQDs, the interactions involved residues such as Thr86, Ile88, Tyr89, Val137, Val145, Tyr147, Phe148, Val149, Gln211, Arg215, Ile218, and others.

Salannol (157144): the docking energy of salannol decreased from -183.108 kcal mol^{-1} to -347.974 kcal mol^{-1} in the presence of GQDs, indicating its enhanced binding affinity (Fig. 9(a and b)). Initially, salannol formed hydrogen bonds with Ile88 and Val149. However, in the presence of GQDs, the hydrogen bonds involved Thr86, Ile88, Tyr89, Thr91, Val145, Val149, and Ile218. In the absence of GQDs, the steric interactions included residues such as Ile88 and Val149. Conversely, in the presence of GQDs, the interactions involved residues such as Thr86, Ile88, Tyr89, Val137, Val145, Tyr147, Phe148, Val149, Gln211, Arg215, Ile218, and others (Table S3) (ESI†).

This comprehensive analysis elucidated the intricate molecular interactions of each compound with *B. subtilis*, highlighting the significant influence of GQDs on their binding affinity and interaction profiles.

4.2.1. Comparative analysis of docking interactions of GQD and twelve compounds with *B. subtilis*. The comparative analysis of the overall results highlights the significant enhancements in the interaction profiles of various compounds with *B. subtilis* upon the addition of GQDs (Fig. 9(a and b)). Overall, there was a notable decrease in the docking energies in the presence of GQDs, indicating the strengthened binding affinities. For instance, compounds such as azadirachtin (PubChem ID: 5281303) demonstrated a decrease in docking energy from -162.11 kcal mol^{-1} to -326.976 kcal mol^{-1}, while that for beta sitosterol (PubChem ID: 222284) showed a decrease from -139.544 kcal mol^{-1} to -304.41 kcal mol^{-1}. This consistent trend underscores the role of GQDs in enhancing the binding affinity of these compounds with *B. subtilis*. Moreover, examining specific molecular interactions provides further insights. The hydrogen bond formations exhibited alterations with the addition of GQDs, as seen in compounds such as mahmoodin (PubChem ID: 126566), where the hydrogen bonds shifted from Asp146 and Asn253 to Thr91, Asp146, Asn253, and Ile257.

Additionally, the steric interactions also showed variations. For instance, in nimbin (PubChem ID: 08058), the steric interactions transitioned from involving residues such as Ile88, Tyr89, Val92, Asp146, Tyr147, and Leu304 without GQDs, to a broader range including Thr86, Ile88, Tyr89, Val137, Val145, Tyr147, Phe148, Val149, Gln211, Arg215, Ile218, Gln219, and Ile257 with GQDs (Fig. 9(a and b)) and (Table S3) (ESI†). Overall, the inclusion of GQDs significantly influenced the interaction profiles of these compounds with *B. subtilis*, resulting in strengthened binding affinities and alterations in specific molecular interactions. These findings underscore the potential of GQDs in enhancing the antibacterial properties of these compounds, suggesting promising avenues for further exploration in the development of antibacterial agents.

4.2.2. Significance of docking interactions: implications for targeted antibacterial drug design against *B. subtilis*.

The comparative analysis of the overall results revealed novel insights into the potential synergistic effects of GQDs when combined with various compounds in their interaction with *Bacillus subtilis*. The significant decrease in docking energies observed for all the compounds upon the addition of GQDs indicates a robust enhancement in their binding affinity. This suggests that GQDs serve as a potent enhancer, potentially amplifying the antibacterial properties of these compounds. Furthermore, the specific alterations in molecular interactions, such as hydrogen bonds and steric interactions, highlight the intricate underlying mechanisms for the synergistic interaction between GQDs and the compounds. The broader range and increased intensity of hydrogen bonds formed in the presence of GQDs suggest a more stabilized and strengthened binding network. Additionally, the diverse array of residues involved in the steric interactions with GQDs indicates a potentially broader spectrum of antibacterial activity. These findings have novel implications for the development of antibacterial strategies. By leveraging the synergistic effects of GQDs, it may be possible to enhance the efficacy of existing antibacterial compounds against *Bacillus subtilis* and potentially other bacterial strains. Moreover, understanding the specific molecular interactions facilitated by GQDs opens avenues for the rational design of novel antibacterial agents with enhanced potency and selectivity. In summary, the overall results underscore the novel significance of GQDs as an enhancer of antibacterial activity and highlight their potential for innovation in the development of next-generation antibacterial therapies. Further exploration of these synergistic interactions may lead to the development of more effective treatments for bacterial infections, addressing an urgent need in healthcare and potentially mitigating the challenges posed by antibiotic resistance.

4.3. Unveiling molecular docking interactions: GQD and twelve compounds with *Aspergillus niger*

Table S4 (ESI†) provides a comprehensive overview of the docking energies and molecular interactions between various compounds and *A. niger*, both with and without the addition of GQDs. Each compound demonstrated distinct patterns of interaction,

shedding light on their potential antibacterial properties and the influence of GQDs.

Azadirachtin (PubChem ID: 5281303) exhibited a significant decrease in docking energy from -72.8779 kcal mol^{-1} to -177.3359 kcal mol^{-1} with the addition of GQDs, suggesting its enhanced binding affinity (Fig. 10(a and b)). Notably, the hydrogen bonds shifted from primarily involving Asn134, Asn341, and Thr441 to Ser133, Asn431, Thr455, Ser457, and Ser460 in the presence of GQDs. Similarly, the steric interactions also underwent a transformation, engaging a broader range of residues such as Asn431, Pro439, His440, and Ser460 with GQDs (Table S4) (ESI†).

Beta sitosterol (PubChem ID: 222284) demonstrated a comparable trend, with a decrease in docking energy from -102.921 kcal mol^{-1} to -207.379 kcal mol^{-1} in the presence of GQDs. The hydrogen bond interactions mainly involved Ser210 without GQDs, while GQDs induced interactions with Ser133, Asn431, Thr455, Ser457, and Ser460. The steric interactions also expanded to include residues such as Ser210, His440, and Thr441 with GQDs (Fig. 10(a and b)) and Table S4 (ESI†).

Catechin (PubChem ID: 9064) exhibited a reduction in docking energy from -81.8352 kcal mol^{-1} to -186.2932 kcal mol^{-1} in the presence of GQDs. The hydrogen bond formations extended to the Ser133, Asn431, Thr455, Ser457, and Ser460 residues, showcasing a diversified interaction network. Similarly, the steric interactions broadened to encompass residues such as Gly127, Ser133, Asn134, Tyr137, and Pro445 in the presence of GQDs.

Epicatechin (PubChem ID: 72276) also displayed a decrease in docking energy from -75.5531 kcal mol^{-1} to -180.0111 kcal mol^{-1} with GQDs. The shift in the hydrogen bond partners to Ser133, Asn431, Thr455, Ser457, and Ser460 indicates strengthened interactions in the presence of GQDs. The steric interactions involved additional residues such as Phe342 and Leu444 with GQDs.
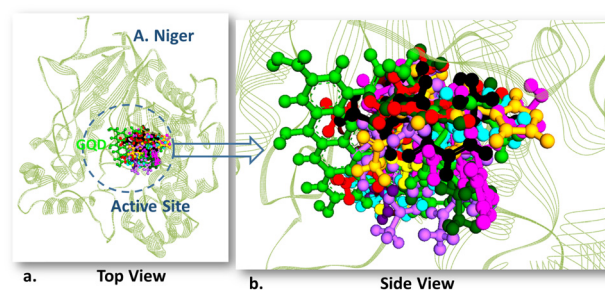

Fig. 10 (a) Top view and (b) side view. Molecular docking interactions of the bacterial receptor (*Aspergillus niger*, PDB ID: 1UKC, represented as a cyan ribbon structure) with graphene quantum dots (GQDs, parrot green color) and 12 bioactive phytochemicals derived from *Azadirachta indica* leaf extract. The ball and stick model representations highlight the GQD-phytochemical complexes: GQD + gallic acid (dark blue), GQD + catechin (red-brown), GQD + nimbolide (violet), GQD + nimbin (red), GQD + mahmoodin (pink), GQD + salannol (olive green), GQD + margolone (yellow), GQD + beta-sitosterol (cyan), GQD + quercetin (white), GQD + gedunin (orange), GQD + nimbolide (black), and GQD + epicatechin (light violet). This detailed depiction elucidates the interface interactions critical for exploring the antibacterial and therapeutic applications of these complexes.

Gallic acid (PubChem ID: 370) exhibited a decrease in docking energy from -60.8918 kcal mol^{-1} to -165.3498 kcal mol^{-1} with GQDs. Notably, the hydrogen bonds in the presence of GQDs encompassed a broader range of residues, including Asn341, Asp428, Pro439, and Gly454. Similarly, the steric interactions involve an expanded set of residues such as Tyr137, Asn341, and Pro445 with GQDs (Fig. 10(a and b)) and Table S4 (ESI†).

Gedunin (PubChem ID: 12004512) demonstrated a reduction in docking energy from -91.0284 kcal mol^{-1} to -195.4864 kcal mol^{-1} with GQDs. The hydrogen bond formations extended to include Ser457 and Ser460 with GQDs, indicating of enhanced interactions. Also, the steric interactions broadened to encompass residues such as Tyr137, Asp428, and Leu444 with GQDs (Fig. 10(a and b)) and Table S4 (ESI†).

Mahmoodin (PubChem ID: 126566) exhibited a decrease in docking energy from -96.9457 kcal mol^{-1} to -201.4047 kcal mol^{-1} with GQDs. The hydrogen bonds extended to involve additional residues such as Ser430 and Tyr462 with GQDs, suggesting augmented interactions. Similarly, the steric interactions encompassed a broader range of residues such as Tyr137, Asp428, and Leu444 with GQDs (Fig. 10(a and b)) and Table S4 (ESI†).

Margolone (PubChem ID: 189728) demonstrated a decrease in docking energy from -77.1733 kcal mol^{-1} to -181.6313 kcal mol^{-1} in the presence of GQDs. The hydrogen bond interactions with GQDs involved an expanded set of residues, including Asn341, Asp428, and His440. Similarly, the steric interactions broadened to include residues such as Tyr137, Ser210, and Leu444 with GQDs (Fig. 10(a and b)) and Table S4 (ESI†).

Nimbin (PubChem ID: 08058) exhibited a reduction in docking energy from -114.573 kcal mol^{-1} to -219.031 kcal mol^{-1} with GQDs. The hydrogen bonds extended to encompass additional residues such as Asn341, Asp428, and His440 with GQDs, indicating enhanced interactions. The steric interactions also broadened to include residues such as Thr441, Leu444, and Thr453 with GQDs (Fig. 10(a and b)) and Table S4 (ESI†).

Nimbolide (PubChem ID: 12313376) demonstrated a decrease in docking energy from -133.588 kcal mol^{-1} to -238.046 kcal mol^{-1} in the presence of GQDs. The hydrogen bond formations extended to involve additional residues such as Thr441 and Ser460 with GQDs, suggesting augmented interactions. The steric interactions also broadened to encompass residues such as Thr441, Leu456, and Ser461 in the presence of GQDs (Fig. 10(a and b)) and Table S4 (ESI†).

Quercetin (PubChem ID: 5280343) exhibited a reduction in docking energy from -78.2364 kcal mol^{-1} to -182.6944 kcal mol^{-1} in the presence of GQDs. The hydrogen bonds extended to involve additional residues such as Gly127, Ser133, and Ser210 in the presence of GQDs, indicating strengthened interactions. The steric interactions also broadened to include residues such as Tyr137, His440, and Pro445 in the presence of GQDs.

Salannol (PubChem ID: 157144) demonstrated a decrease in docking energy from -99.399 kcal mol^{-1} to -203.857 kcal mol^{-1} in the presence of GQDs. The hydrogen bond formations extended to encompass additional residues such as Asn341 and Ser457, suggesting enhanced interactions. The steric interactions also broadened to include residues such as His440, Phe442, and Leu444 with GQDs (Fig. 10(a and b)) and Table S4 (ESI†).

Overall, the incorporation of GQDs led to significant enhancements in the interaction profiles of these compounds with *A. niger*, indicating their potential for synergistic antibacterial effects and highlighting avenues for further research and development in antifungal therapy.

4.3.1. Comparative analysis of docking interactions of GQD and twelve compounds with *A. niger*. Table S4 (ESI†) presents a comparative analysis of the docking energies, hydrogen bond formations, and steric interactions of the various compounds with *A. niger*, both in the presence and absence of GQDs. Examining the overall results revealed several noteworthy observations across the compounds studied. Firstly, there was a consistent decrease in docking energies for all the compounds when GQDs were introduced. For example, azadirachtin (PubChem ID: 5281303) exhibited a decrease in docking energy from -72.8779 kcal mol^{-1} to -177.3359 kcal mol^{-1} in the presence of GQDs, indicating enhanced binding affinity. This trend was also observed across the other compounds such as beta sitosterol (PubChem ID: 222284) and catechin (PubChem ID: 9064), emphasizing the general strengthening effect of GQDs on compound binding to *Bacillus subtilis* (Fig. 10(a and b)) and Table S4 (ESI†). Moreover, the alterations in hydrogen bond formations and steric interactions further underscore the impact of GQDs on the molecular interactions. For instance, azadirachtin formed hydrogen bonds with Asn134, Asn341, and Thr441 in the absence of GQDs, whereas in the presence of GQDs, additional hydrogen bonds were formed with Ser133, Asn431, Thr455, Ser457, and Ser460. Similarly, the steric interactions involving azadirachtin shifted from primarily involving Asn134, Asn341, Asn431, Pro439, His440, Thr441, Pro445, Thr453, and Leu456 to a broader range of residues with GQDs, including Ser133, Asn341, Asp428, Asn431, Pro439, His440, Thr453, Gly454, Thr455, Leu456, Ser457, and Ser460. Overall, the comparative analysis highlights the significant influence of GQDs on the interaction profiles of the studied compounds with *A. niger*. The consistent decrease in docking energies and the alterations in specific molecular interactions suggest that GQDs play a crucial role in enhancing the binding affinity and modulating the interaction network between the compounds and *A. niger*. These findings provide valuable insights into the potential application of GQDs as enhancers of antibacterial activity and pave the way for further research in the development of novel antifungal therapies.

4.3.2. Significance of docking interactions: implications for targeted antibacterial drug design against *A. niger*. The overarching significance of the overall results is their implications for the development of innovative antifungal strategies leveraging GQDs. The observed decrease in docking energies across various compounds in the presence of GQDs signifies a promising avenue for enhancing the efficacy of antifungal agents against *A. niger*. This enhancement in binding affinity suggests that GQDs have the potential to serve as potent enhancers, augmenting the antifungal properties of existing compounds and potentially expanding their applicability in

combating fungal infections. Furthermore, the alterations in hydrogen bond formations and steric interactions underscore the multifaceted impact of GQDs on the molecular interaction landscape. By facilitating the formation of additional hydrogen bonds and influencing steric interactions, GQDs may contribute to the stabilization of compound-fungus complexes and the disruption of bacterial mechanisms, ultimately leading to improved antifungal efficacy. The novel importance of these findings is their potential to address the pressing global challenge of antibiotic resistance. By harnessing the synergistic effects of GQDs, it may be possible to develop antifungal therapies that are not only more effective but also less prone to resistance development. Additionally, the versatility of GQDs opens avenues for the design of tailored antifungal agents with enhanced specificity and reduced side effects. In summary, the overall results underscore the novel importance of GQDs as promising enhancers of antifungal activity. These findings pave the way for further research into the development of GQD-based antifungal therapies, offering new hope in the fight against fungal infections and antibiotic resistance.

4.4. Pharmacophore modeling and feature extraction

Fig. S1 and Table S5 (ESI)† present the pharmacophore features of twelve compounds derived from *A. indica*, commonly known as neem, together with GQDs. Each compound is characterized by its hydrogen bond acceptor, hydrogen bond donor, hydrophobic, ring aromatic, and negative ionizable properties.

Azadirachtin, a prominent bioactive compound found in neem, exhibits a high number of hydrogen bond acceptors and donors, indicating its potential for forming strong interactions with biological molecules. It also shows a moderate hydrophobic nature. Beta sitosterol, another compound present in neem, demonstrates balanced hydrogen bonding and hydrophobic characteristics, which can contribute to its diverse biological activities. Catechin and epicatechin, both flavonoids, exhibit significant hydrogen bonding capabilities together with moderate hydrophobicity and aromaticity, suggesting their potential antioxidant properties. Gallic acid, known for its antioxidant and anti-inflammatory effects, displays notable hydrogen bonding and moderate hydrophobicity. Gedunin and nimbin, limonoids found in neem, exhibit varying degrees of hydrogen bonding and hydrophobicity, indicating their potential as anticancer agents. Mahmoodin, a triterpenoid, demonstrates considerable hydrogen bonding and hydrophobic properties, possibly contributing to its pharmacological activities. Margolone, a limonoid, shows moderate hydrogen bonding and significant hydrophobicity, suggesting its potential as an antimalarial agent. Nimbolide, another limonoid, displays similar pharmacophore features to margolone, highlighting its potential therapeutic effects. Quercetin, a flavonoid present in neem, exhibits substantial hydrogen bonding and aromatic properties, indicating its antioxidant and anti-inflammatory potential. Salannol, a neolignan compound, shows significant hydrogen bonding and hydrophobicity, suggesting its potential as an anti-inflammatory agent. Finally, GQDs demonstrate a high degree of hydrogen bonding, hydrophobicity, and moderate hydrogen bond donation and accepting ability, indicating their potential applications in drug delivery and bioimaging. Overall, the pharmacophore features outlined in Fig. S1 and Table S5 (ESI†) provide valuable insights into the diverse biological activities of *A. indica* compounds and GQDs, offering avenues for their further exploration in drug discovery and development.

4.4.1. Comparative analysis of pharmacophore features in twelve compounds and graphene quantum dots (GQD) for potential drug-receptor interactions. In the comparison of the pharmacophore features of the compounds derived from *A. indica* and GQDs, several patterns emerged, as shown in Fig. S1 and Table S5 (ESI†). *A. indica* compounds exhibit diverse characteristics, with varying degrees of hydrogen bond acceptors, hydrogen bond donors, hydrophobicity, aromaticity, and negative ionizability. Azadirachtin, its prominent bioactive compound, stands out with a high number of hydrogen bond acceptors and donors, indicating its strong potential for molecular interactions. Flavonoids such as catechin, epicatechin, and quercetin also exhibit significant hydrogen bonding and aromatic properties, suggesting their antioxidant and anti-inflammatory potential. Alternatively, limonoids such as gedunin, nimbin, and nimbolide demonstrate moderate hydrogen bonding and hydrophobicity, potentially contributing to their anticancer and therapeutic effects. Triterpenoids such as mahmoodin exhibit considerable hydrogen bonding and hydrophobic properties, highlighting their pharmacological activities. Neolignans such as salannol show significant hydrogen bonding and hydrophobicity, indicating their potential anti-inflammatory effects. In contrast, GQDs demonstrate a uniform pharmacophore profile with a high number of hydrogen bond acceptors and donors, as well as significant hydrophobicity. This suggests their potential applications in drug delivery and bioimaging, where strong interactions with biological molecules and cellular membranes are essential. Overall, although the *A. indica* compounds exhibit diverse pharmacophore features reflecting their multifaceted biological activities, GQDs present a more consistent profile suitable for specific biomedical applications. This comparison underscores the potential of both natural compounds from *A. indica* and nanomaterials such as GQDs in pharmaceutical research and development, offering complementary avenues for drug discovery and therapeutic innovation.

4.4.2. Significance of pharmacophoric diversity in twelve compounds and graphene quantum dots (GQD) for targeted drug design. The comprehensive analysis of the pharmacophore features of the *A. indica* compounds and GQDs yielded novel insights with significant importance and implications. Firstly, the diversity of the pharmacophore features among the *A. indica* compounds underscores the rich biochemical profile of this natural resource. By elucidating the specific molecular interactions facilitated by each compound, these findings pave the way for targeted drug design and optimization. Harnessing the unique pharmacophore characteristics of *A. indica* compounds can lead to the development of novel therapeutics targeting various diseases, including cancer, inflammation, and infectious diseases. Secondly, the uniform pharmacophore profile observed in GQDs highlights their potential as versatile nanomaterials with broad biomedical applications. Their high

number of hydrogen bond acceptors and donors, together with significant hydrophobicity positions GQDs as promising candidates for drug delivery systems, imaging agents, and biosensors. The consistency in pharmacophore features across GQDs also simplifies their integration into drug formulations and biomedical devices, streamlining research and development processes. Moreover, the comparison between natural compounds from *A. indica* and synthetic nanomaterials such as GQDs underscores the synergy between traditional pharmacology and nanotechnology. By combining the unique properties of natural compounds with the tailored characteristics of nanomaterials, researchers can develop innovative solutions that address unmet medical needs more effectively. This interdisciplinary approach not only enhances the therapeutic potential of *A. indica* compounds but also expands the utility of nanomaterials in biomedicine. Overall, the novel importance of these results is their potential to drive drug discovery and biomedical innovation forward. By elucidating the pharmacophore features of *A. indica* compounds and GQDs, this research sets the stage for the development of next-generation therapeutics and biomedical technologies with enhanced efficacy, specificity, and safety profiles.

4.5. Density functional theory (DFT) and molecular electrostatic potential (MESP) calculations

Azadirachtin (PubChem ID: 5281303): azadirachtin exhibited a moderate band gap energy (0.116233 eV) and a significant dipole moment (2.08915 Debye) before the addition of GQDs. The addition of GQDs induced a noteworthy decrease in its band gap energy (0.00241189 eV), suggesting enhanced electronic communication. The dipole moment remained relatively stable, implying that this compound maintained its polarity despite the structural modifications (Fig. S2 and Table S6 (ESI†)).

Beta sitosterol (PubChem ID: 222284): beta sitosterol displays a wider band gap energy (0.193036 eV) compared to azadirachtin and a lower dipole moment (0.855187 Debye). The introduction of GQDs resulted in a minimal change in the band gap energy (0.00098168 eV). This implies that beta sitosterol, with its already substantial band gap, may have limited electronic interactions with GQDs (Fig. S2 and Table S6 (ESI†)).

Catechin (PubChem ID: 9064): catechin shares similarities with azadirachtin in terms of band gap energy (0.149653 eV) and dipole moment (1.04997 Debye). After the addition of GQDs, its band gap energy decreased slightly (0.00240679 eV), indicating the increase in potential for electronic interactions. Alternatively, its dipole moment remained consistent, suggesting that this compound retained its inherent polarity (Fig. S2 and Table S6 (ESI†)).

Epicatechin (PubChem ID: 72276): epicatechin has a moderate band gap energy (0.141289 eV) and a smaller dipole moment (0.306641 Debye) compared to that of azadirachtin and catechin. The addition of GQDs induced a subtle decrease in its band gap energy (0.00137426 eV). Its relatively smaller dipole moment may contribute to less pronounced interactions with GQDs compared to other compounds (Fig. S2 and Table S6 (ESI†)).

Gallic acid (PubChem ID: 370): gallic acid has a larger dipole moment (0.873523 Debye) and moderate band gap energy (0.12184 eV). After the addition of GQDs, a slight decrease in its band gap energy (0.00145018 eV) was observed. The notable dipole moment of gallic acid suggests that it maintains its polarity, possibly influencing its interactions with GQDs (Fig. S2 and Table S6 (ESI†)).

Gedunin (PubChem ID: 12004512): gedunin exhibits a substantial dipole moment (2.58204 Debye) and a moderate band gap energy (0.102568 eV). The addition of GQDs induced a noticeable increase in its band gap energy (0.0051582 eV), indicating its reduced potential for electronic interactions. The significant dipole moment suggests that the inherent polarity of gedunin remained robust (Fig. S2 and Table S6 (ESI†)).

Mahmoodin (PubChem ID: 126566): mahmoodin displays a moderate band gap energy (0.102732 eV) and dipole moment (1.91576 Debye). After the addition of GQDs, its band gap energy slightly increased (0.00175331 eV). This compound retained a considerable dipole moment, indicating that its polarity was preserved during its interaction with GQDs (Fig. S2 and Table S6 (ESI†)).

Margolone (PubChem ID: 189728): margolone has a moderate dipole moment (1.96214 Debye) and band energy (0.106498 eV). The addition of GQDs induced a minor change in its band gap energy (0.00213628 eV), suggesting subtle modifications in its electronic interactions. The relatively large dipole moment of this compound indicates its inherent polarity (Fig. S2 and Table S6 (ESI†)).

Nimbin (PubChem ID: 08058): nimbin possesses a smaller dipole moment (0.662956 Debye) and band gap energy (0.0841336 eV) compared to the other compounds. After the addition of GQDs, its band gap energy significantly decreased (0.00306017 eV). This indicates increased electronic communication, despite its smaller dipole moment (Fig. S2 and Table S6 (ESI†)).

Nimbolide (PubChem ID: 12313376): nimbolide has a substantial dipole moment (2.85011 Debye) and a relatively small band gap energy (0.0786596 eV). After the addition of GQDs, its band gap energy increased slightly (0.00334654 eV). The significant dipole moment suggests that nimbolide maintained its polarity, potentially influencing its interactions with GQDs.

Quercetin (PubChem ID: 5280343): quercetin demonstrates moderate band gap energy (0.108986 eV) and dipole moment (2.18812 Debye). The addition of GQDs induced a slight decrease in band gap energy (0.00801342 eV), suggesting enhanced electronic interactions. The substantial dipole moment indicates that quercetin retained its inherent polarity during its interaction with GQDs (Fig. S2 and Table S6 (ESI†)).

Salannol (PubChem ID: 157144): salannol exhibits a moderate band gap energy (0.132503 eV) and a smaller dipole moment (1.78229 Debye). After the addition of GQDs, its band gap energy slightly decreased (0.00188333 eV), indicating potential modifications in its electronic interactions. The dipole moment of salannol suggests that its inherent polarity remained intact (Fig. S2 and Table S6 (ESI†)).

These detailed discussions highlight the nuanced changes in electronic properties for each compound before and after the addition of graphene quantum dots, providing insights into their potential interactions and reactivity.

4.5.1. Comparison of density functional theory results. According to the comparison of the overall results for each compound before and after the addition of GQDs (Fig. S2 and Table S6 (ESI†)), several trends and patterns emerge.

(a) Band gap energy. The addition of GQDs generally led to a decrease in the band gap energy of most of the compounds. This suggests an increased potential for electronic communication and improved conductivity in the presence of GQDs.

(b) Dipole moment. The dipole moment, which indicates the polarity of the compounds, remained relatively stable for many of the compounds after the addition of GQDs. This implies that the interactions of the molecules with GQDs do not significantly alter their inherent polarity.

(c) Hardness and softness. The hardness and softness values, which provide insights into the stability and reactivity of compounds, showed minor changes in response to the addition of GQDs. The compounds generally maintained their characteristic hardness and softness.

(d) Electronegativity and electrophilicity. The electronegativity values exhibit slight variations, reflecting subtle changes in the ability of the compounds to attract electrons. The electrophilicity values also show minor adjustments, indicating reactivity of the compounds toward nucleophiles.

(e) Individual compound responses. The compounds with larger initial dipole moments (*e.g.*, gedunin and nimbolide) tended to maintain their polarity after the addition of GQDs. The compounds with moderate band gap energies (*e.g.*, azadirachtin and catechin) showed noticeable changes in their band gap, suggesting enhanced electronic interactions with GQDs. The compounds with smaller dipole moments (*e.g.*, nimbin) experienced significant changes in their band gap energy, indicating potential modifications in electronic properties.

(f) Overall trends. The influence of GQDs on electronic properties appears to be compound-specific, with some compounds exhibiting more pronounced changes than others. Although the band gap energies generally decreased, indicating improved electronic communication, the impact on other properties varied, highlighting the complex nature of the interactions between GQDs and different compounds.

In summary, the addition of GQDs tended to influence the band gap energies, with varying effects on the other electronic properties. The individual responses of each compound highlight the need for a nuanced understanding of the interaction between specific molecules and GQDs, considering factors such as initial polarity, band gap energy, and inherent reactivity.

4.5.2. Electronic structure analysis and reactivity potential of synthesized GQDs + 12 compounds *via* density functional theory (DFT) calculations. The electronic structure analysis and reactivity potential provide valuable insights into how the addition of GQDs influenced the electronic properties and chemical reactivity of the compounds. Here, we present a discussion on these aspects based on the overall results.

(a) Band gap energy modification. The overall trend of a decrease in band gap energy after the addition of GQDs indicates the narrowing of the energy gap between the highest occupied molecular orbital (HOMO) and lowest unoccupied molecular orbital (LUMO). This suggests that GQDs facilitate electron transfer processes, potentially enhancing the conductivity and electronic communication within the compounds.

(b) Dipole moment stability. Despite the changes in other electronic properties, the dipole moment generally remained stable for many of the compounds after the addition of GQDs. This suggests that the inherent polarity of the molecules was preserved, indicating that the interactions with GQDs do not alter their overall charge distribution significantly.

(c) Electronegativity and electrophilicity variations. The minor variations in electronegativity and electrophilicity values indicate subtle changes in the ability of the compounds to attract electrons and their reactivity toward nucleophiles. These changes may arise from adjustments in their electron density due to GQD interactions.

(d) Enhanced reactivity. The decrease in band gap energy suggests an increased potential for electronic interactions and reactivity. The compounds with smaller band gaps may exhibit enhanced reactivity, facilitating electron transfer processes and promoting chemical transformations.

(e) Polarity and reactivity. The stability of the dipole moments indicates that the addition of GQDs did not significantly alter the overall polarity of the compounds. However, the compounds with larger initial dipole moments may retain their reactivity toward polar solvents and other molecules, influencing their chemical behavior.

(f) Softness and electrophilicity. Although the hardness and softness values remained relatively stable, the minor changes in electrophilicity suggest subtle variations in the reactivity of the compounds toward nucleophiles. The compounds with higher electrophilicity values may exhibit increased susceptibility to nucleophilic attack, leading to enhanced chemical reactivity.

Overall, the electronic structure analysis indicates that the addition of GQDs influences the electronic properties of the compounds, primarily through modifications in their band gap energies and electron distribution. These changes have implications in the reactivity potential of the compounds, with potential for enhanced electronic communication and chemical transformations in the presence of GQDs. However, the specific effects vary depending on the individual characteristics of the compounds, highlighting the importance of considering compound-specific interactions in understanding reactivity potential.

4.5.3. Molecular electrostatic potential (MESP) analysis. The assessment of molecular electrostatic potential (MESP) provides valuable insights into the electrostatic characteristics of various compounds and their interactions with GQDs. The use of color-coded electrostatic potential maps allows a comprehensive examination of the molecular sites susceptible to electrophilic attack, nucleophilic reactivity, and hydrogen bonding interactions (Fig. S3 (ESI†)). Thus, the MESP analyses conducted on the lead compounds shed light on their electrostatic features.

In the case of the azadirachtin + GQD complex compound, the electrostatic potential is nearly neutral due to the cancellation of the net negative charge of azadirachtin and the net positive charge of GQDs. This suggests weak electrostatic interactions between the components, primarily van der Waals forces. In contrast, the beta-sitosterol + GQD complex compound likely exhibits a negative potential around beta-sitosterol, which is attracted to the positive charges on the edges of GQDs. The hydroxyl group at position 3 of beta-sitosterol contributes to its negative charge, enhancing its interactions with GQDs. Similarly, the catechin + GQD and epicatechin + GQD complex compounds are expected to display negative potentials around catechin and epicatechin, respectively, due to their net negative charges, fostering attractive interactions with the positively charged GQDs. The gallic acid + GQD complex compound is anticipated to have a negative potential, with the negatively charged gallic acid attracted to the positively charged edges of GQDs. However, the specific distribution of potential within the complex can be influenced by solvent interactions and pH variations. In the case of the gedunin + GQD complex compound, the negative potential around gedunin is likely attracted to the positive edges of GQDs, resulting in an overall negative potential. The close contact between gedunin and GQDs may strengthen the electrostatic interactions. In the case of the mahmoodin + GQD complex compound, the neutral or slightly negative potential of mahmoodin may weakly interact with the negatively charged GQDs, potentially attenuating their negative charge, although the overall potential remains predominantly negative.

The margolone + GQD complex compound, where both components carry a net negative charge, may exhibit weak or repulsive interactions, making predictions challenging due to the complexity of the interactions and structural arrangements. In the nimbolide + graphene quantum dot complex compound, the interaction depends on whether GQDs carry a net positive or negative charge. The positive GQDs can result in a near-neutral potential, while negative GQDs may yield a more negative overall potential. In the quercetin + GQD complex compound, the repulsive interactions between negatively charged components may lead to a more negative potential, although the π–π stacking interactions between aromatic rings can contribute to stability. Lastly, in the case of the salannol + GQD complex compound, the repulsive interactions between the negatively charged components may dominate, potentially resulting in a negative overall potential, influenced by solvent effects, pH, and specific salannol structure. Overall, although these predictions provide insights into the electrostatic potentials of the complex compounds, the dynamic nature of the molecular interactions and environmental factors necessitate further investigation for a comprehensive understanding.

4.5.3.1. Comparative analysis of electrostatic potential maps reveals molecular variations in synthesized GQDs + 12 compounds. According to the comparison of the overall results of the various complex compounds with GQDs, several trends and differences emerge regarding their molecular electrostatic potentials. Firstly, although some complexes such as beta-sitosterol, catechin, epicatechin, gallic acid, gedunin, and mahmoodin tend to exhibit negative electrostatic potentials, indicating attractive interactions with the positively charged GQDs, others such as azadirachtin showed a neutral potential due to charge cancellation. This disparity highlights the importance of considering the specific chemical properties of both the compound and the GQDs when assessing their interactions. Moreover, the structural characteristics of the compounds play a significant role in determining their electrostatic potentials. The compounds with multiple hydroxyl groups, such as beta-sitosterol, catechin, epicatechin, gallic acid, gedunin, and mahmoodin, tended to display negative potentials, reflecting the influence of these charged functional groups on their overall charge distribution. Conversely, compounds such as azadirachtin and nimbolide, which lack abundant charged groups, were more prone to yielding neutral or less negative potentials. Additionally, the presence of π–π stacking interactions, as observed in the quercetin + GQD complex, can potentially influence the overall electrostatic potential, providing an additional stabilizing factor despite the repulsive interactions between the negatively charged components. Lastly, the complexity of the interactions is evident in the salannol + GQD complex, where repulsive electrostatic interactions are expected due to the similarly charged components, underscoring the need for a nuanced understanding of the molecular interactions in heterogeneous systems. Overall, although common trends such as negative potentials predominating in the complexes with hydroxyl-rich compounds were observed, the specific characteristics of each compound and its interaction with GQDs dictate the resultant electrostatic potential, emphasizing the inherent complexity in these systems.

4.6. Unveiling unique molecular signatures: electrostatic potential maps in diverse synthesized GQDs + 12 compounds

The novel importance of the overall results is their implication for the design and development of functional materials and systems based on GQDs and complex compounds. Understanding the molecular electrostatic potentials of these complexes offers valuable insights into their stability, reactivity, and potential applications across various fields.

One significant implication is in the realm of nanotechnology and materials science, where the ability to manipulate the electrostatic interactions between GQDs and complex compounds can lead to the development of novel materials with tailored properties. By modulating the electrostatic potential, researchers can engineer materials with enhanced stability, improved adsorption capabilities, and optimized electronic

properties, thus opening avenues for the fabrication of advanced sensors, catalysts, and energy storage devices. Moreover, the insights gained from the electrostatic characterization of these complexes can inform the design of drug delivery systems and biomedical applications. Understanding how different compounds interact with GQDs on a molecular level can guide the development of targeted drug delivery vehicles with improved biocompatibility and efficacy. Additionally, it can aid in the design of bioimaging agents and theranostic platforms for simultaneous diagnosis and therapy. Furthermore, the ability to predict and control the electrostatic interactions between GQDs and complex compounds has implications for environmental remediation and pollution control. By harnessing these interactions, researchers can develop efficient adsorbents for removing pollutants and contaminants from the air and water sources, contributing to efforts towards sustainable environmental management. Overall, the novel importance of these results is their potential to inspire the creation of innovative technologies and solutions that address pressing societal challenges across multiple domains, ranging from healthcare and materials science to environmental sustainability. By leveraging our understanding of molecular electrostatic potentials, we can unlock new opportunities for technological advancement and societal benefit.

4.7. Absorption, distribution, metabolism, excretion, and toxicity(ADMET) analysis

The results outlined in the ADMET table offer a detailed assessment of the various pharmacokinetic and toxicological parameters associated with the twelve investigated compounds including azadirachtin, beta-sitosterol, catechin, epicatechin, gallic acid, gedunin, mahmoodin, margolone, nimbolide, quercetin, salannol, and GDQs (Table S7 (ESI†)). These parameters play a crucial role in understanding how these compounds interact within biological systems, influencing their toxicological effects and bioavailability. Specifically, this table meticulously delineates parameters such as "ADMET-EXT-CYP2D6," which provides insights into the association of the compounds with cytochrome P450 2D6 (CYP2D6), a crucial enzyme in drug metabolism. The data showcases a spectrum of values across the compounds, indicating varying levels of potential interactions with this enzyme. Moreover, the "ADMET-EXT-CYP2D6#prediction" column offers valuable insights into the likelihood of specific toxicological outcomes, providing a comprehensive overview of the CYP2D6-related properties of the compounds. Additionally, the evaluation of parameters such as "ADMET-EXT-CYP2D6-Applicability" enriches the understanding of the toxicological profiles of the compounds by assessing whether their properties and operational parameters are consistent with expected ranges concerning CYP2D6. The findings suggest favorable applicability across most compounds, enhancing confidence in their safety profiles. Furthermore, the assessment of hepatotoxicity, absorption levels, plasma protein binding (PPB), AlogP98, and 2D polar surface area (PSA) offers valuable insights into the compounds' pharmacokinetic properties and potential biological activities. The results indicate varying levels of solubility, BBB penetration, and PPB among the compounds, highlighting their diverse pharmacological profiles. Notably, compounds such as mahmoodin, margolone, nimbolide, and salannol are not predicted to be hepatotoxic, while others such as quercetin and GDQs exhibit potential hepatotoxicity (Table S7 (ESI†)). Additionally, the differences in absorption levels and PPB predictions further underscore the variability in the pharmacokinetic behavior of the compounds. In conclusion, the comprehensive evaluation provided by the ADMET table serves as a valuable tool in guiding the further exploration and development of the evaluated compounds for potential therapeutic applications.

Beyond the individual assessments of each compound, the overall results presented in the ADMET table offer novel insights into the collective pharmacokinetic and toxicological landscape of the synthesized metal compounds. By examining the ensemble of parameters across all compounds, patterns and trends emerge that may not be immediately apparent when considering each compound in isolation. One novel importance is the identification of commonalities and differences among the compounds. For instance, although some compounds exhibit similar solubility levels or BBB penetration capabilities, others may show distinct profiles. Understanding these shared characteristics and disparities can inform the development of strategies for optimizing drug formulation or targeting specific biological pathways. Moreover, the collective results shed light on potential synergistic effects or adverse interactions that may arise from the co-administration of multiple compounds. By comprehensively assessing parameters such as CYP2D6 metabolism, hepatotoxicity, and plasma protein binding across all compounds, researchers can anticipate and mitigate potential drug-drug interactions, thereby enhancing the safety and efficacy of combination therapies. Furthermore, the overall results underscore the importance of considering multiple factors in drug development and design. Although solubility and BBB penetration are crucial for drug bioavailability and central nervous system targeting, factors such as metabolism and hepatotoxicity play pivotal roles in drug safety and tolerability. By integrating diverse parameters into a unified analysis, researchers can gain a more holistic understanding of the pharmacological properties and potential risks associated with compounds, guiding informed decision-making throughout the drug development process. In essence, the novel importance of the overall results is their capacity to provide a comprehensive and integrative perspective on the pharmacokinetic and toxicological characteristics of synthesized metal compounds, offering valuable guidance for optimizing their therapeutic potential and minimizing potential adverse effects in clinical applications.

5. Experimental sections

5.1. Plant material identification

Azadirachta indica (locally known as Neem) leaves were collected from the Herbal Garden of Maharshi Dayanand University, Rohtak. This was confirmed and certified by CSIR-NIScPR. New Delhi (Specimen voucher number Ref. No. NIScPR/RHMD/ 2022/4021-22-1). The collected leaves were washed to eliminate

dust particles and dried for 12 days in the shade to eradicate moisture. Subsequently, the dehydrated leaves were crushed into a fine powder.

5.1.1. Chemicals, reagents and microorganisms. Butylated hydroxyl toluene, sodium phosphate, 2,2-diphenyl—picrylhydrazyl (DPPH), Muller-Hinton broth, Muller-Hinton agar, Sabouraud dextrose agar, streptomycin, amphotericin B disc, ethanol (99.9%), methanol, and sulfuric acid (98%), deionized water, *B. Subtilis* (MTCC 121), *P. aeruginosa* (MTCC 424), *S. aureus* (MTCC 96), *E. coli* (MTCC 443), *Aspergillus flavus* (MTCC 277), *Aspergillus niger* (MTCC 281) and neem leaf extract were used throughout the experimental work.

5.1.2. Apparatus and instruments. Hot plate with magnetic stirrer, mortar and pestle, graduated cylinders, beakers, electric grinder, domestic microwave (900 W), UV-Visible spectrometer (Shimadzu, UV 3600 Plus), XRD (Rigaku, Smart Lab 3 kW), FESEM-EDX (JEOL, 7610F Plus), HRTEM (TECNAI, 200 kV), FTIR (MB 3000 ABB), zeta potential (Malvern, Nano ZS).

5.1.3. Synthesis protocol of plant leaf extract & GQDs. The maceration process was used for extraction.[27] Briefly, 20 g of leaf powder was dissolved in 200 mL absolute ethanol and allowed to stand at room temperature for 48 h. Subsequently, the resulting filtrate was filtered using Whatman filter paper No. 1, and the dried extracts were preserved for future use at −4 °C.

The green synthesis of GQDs was carried out using the methodology reported by Kumawat *et al.*, with certain modifications.[18,28] Briefly, 20 g of *Azadirachta indica* leaf powder was dissolved in 200 mL of absolute ethanol and stirred continuously for 4 h using a magnetic stirrer at room temperature. Then, the extract was centrifuged at 5000 rpm for 12 min to get a clear solvent. The solvent was concentrated using a rotary evaporator and the resulting thick slurry was combined with a 2 mL of Milli Q water, and further, the mixture was heated in a domestic microwave oven (900 W) for 6 min. Then, the residue was dispersed using 99.9% ethanol and filtered through a 0.22 μm syringe filter to extract pure GQDs. The dried powder was preserved at −4 °C for future use. A UV-Visible spectrophotometer, FTIR, XRD, TEM, SEM, and zeta potential analyzer were used to characterize the synthesized GQDs.

5.1.4. Elemental composition analysis – complementing EDX with XPS/EELS. To determine the elemental composition of the synthesized GQDs, we utilized energy-dispersive X-ray (EDX) analysis. However, it is recognized that EDX has limitations in accurately detecting light elements such as carbon and oxygen. Therefore, X-ray photoelectron spectroscopy (XPS) or electron energy loss spectroscopy (EELS) could serve as complementary analyses to provide a more reliable elemental characterization, particularly for the surface functional groups involving light elements. For instance, XPS allows more precise identification of specific chemical states and bonding configurations, which are important for confirming the presence of oxygen-containing functionalities such as hydroxyl and carboxyl groups on GQDs. Recent studies have successfully employed XPS to verify the composition and functional groups in carbon-based nanomaterials, thereby supporting our approach.[29,30]

5.2. Biological experiments

In vitro, DPPH free radical scavenging assay, agar well diffusion, disc diffusion and microplate reader assays were carried out against the synthesized GQDs and ethanolic leaf extract in an effort to identify a significant agent for infectious diseases.

5.2.1. DPPH free radical scavenging assay. Free radicals emerge by several biological mechanisms. One of the foremost fields of research and application of nanomaterials is getting rid of these free radicals that are generated when biomolecules encounter molecular oxygen. (1) The diphenyl-1-picrylhydrazyl free radical scavenging assay was used for evaluating the antioxidant effectiveness of the neem leaf extract and GQDs.[31] About 100 μL of 0.05 mg mL^{-1} DPPH was mixed to test the samples (20, 40, 60, 80, and 100 μg mL^{-1}). After 30 min of incubation in the dark, the absorbance at 517 nm was measured using ascorbic acid as a standard.

$$\text{DPPH radical scavenging } (\%) = \frac{(\text{Absorbance of control} - \text{Absorbance of test sample}) \times 100}{\text{Absorbance of control}}$$

5.2.2. Agar well diffusion assay. Agar well diffusion was used to assess the antibacterial activity of the synthesized GQDs and leaf extract against bacterial strains procured from the Department of Microbiology at Maharshi Dayanand University, Rohtak, India.[32] The bacteria were grown in Muller-Hinton Broth, and the turbidity was adjusted to match the 0.5 McFarland standard. Nutrient broth was used to create the inoculum, which was then incubated for 24 h at 36 °C ± 1 °C in a shaking incubator. To get 1.5 × 10^8 CFU mL^{-1}, the culture was diluted with 0.9% saline solution. Each culture was allocated independently on MHA plates by sterilized swab. After inoculation, 100 μL of sample (6.25, 12.5, 50, and 100 mg mL^{-1}) was poured into wells that were previously perforated with a cork borer. Streptomycin and rifamycin were used as a positive control. The zone of inhibition was assessed for test samples following 24 h incubation at 37 °C.

5.2.3. Disc diffusion assay (antimicrobial activity). The disc diffusion method was used to assess the antifungal activity of the produced GQDs and leaf extract.[33] Microbial cultures were employed to inoculate Sabouraud dextrose agar medium plates. Using sterile forceps, sterile discs measuring 6 mm in diameter were inserted. GQDs and neem leaf ethanolic extract of various concentration (6.25, 12.5, 50, 100 mg mL^{-1}) were applied on discs amphotericin B disc used as positive control. The zone of inhibition was evaluated after incubation for 24 h.

5.2.4. MIC assay. To determine the minimum inhibitory concentration (MIC) capable of stopping the development of bacteria, we performed an experiment in which resazurin undergoes a colour shift. After being combined with MHB, the test samples were added to column 1 and progressively diluted until column 11. Then 10 μL of the standard microbial solution was added to each well, yielding 105 CFU mL^{-1}. Column 12, which served as the control, only included the bacterial suspension. Following a 24-h period, 10 μL of 0.5 mg mL^{-1} resazurin in DI was introduced in each well (ranging from rows A to D).

Then, the resultant cultures were incubated for three hours at 37 °C. The minimum inhibitory concentration (MIC) of the test samples was found to be the amount that prevented a colour change in resazurin.

5.3. Computational methodology

5.3.1. Unveiling the nexus: exploring protein binding sites. In the quest to uncover the intricacies of the protein binding sites, the Computed Atlas of Surface Topography of Proteins (CASTp) server[34] has emerged as a beacon of precision and insight. This web-based tool has been meticulously crafted for the precise prediction of the active sites in proteins, delving deep into the labyrinth of 3D protein structures to unravel their secrets. With adept precision, CASTp navigates the intricate folds of proteins, deftly identifying and evaluating pockets and voids with unparalleled accuracy. Not content with mere measurements, it offers a comprehensive analysis of their spatial dimensions, encompassing both area and volume. Furthermore, CASTp goes beyond the surface, providing detailed insights into the composition of the active site. Here, it meticulously delineates the specific amino acids that contribute to its formation, unveiling their precise spatial coordinates.[35]

Armed with the insights gleaned from CASTp, our journey into the realm of docking analysis begins. With discerning eyes, we judiciously selected the most promising binding pockets unearthed by CASTp, prioritizing those endowed with a significant area and volume. These designated pockets, identified as potential active sites, serve as the focal points for further exploration and investigation. In the nexus between the precision of CASTp and our strategic selection, the promise of unraveling the mysteries of the protein binding sites is significant. With each designated pocket, we embark on a journey of discovery, unraveling the intricate dance between proteins and ligands, inching closer to unlocking the secrets of biological interaction.

5.3.2. Harnessing graphene quantum dots (GQD) and ligand preparation for molecular docking simulations. In our quest for precise and dependable outcomes, we embarked on a meticulous journey to prepare GQDs and ligands for molecular docking simulations. Our methodology unfolded with the retrieval of three-dimensional structures of GQD and neem compounds from PubChem, a cornerstone database renowned for housing 3D chemical structures in.SDF format. These initial structures served as the bedrock for subsequent refinement and optimization. Next, the obtained structures traversed a crucial optimization phase leveraging the prowess of AutoDock Tools, a specialized software suite meticulously tailored for preparing molecules for docking simulations. Here, our focus shifted to refining the structures of GQD and compounds to usher them into an energetically favorable and conducive state for interaction with the target protein. Within the realm of AutoDock Tools, a symphony of adjustments ensued as various parameters were fine-tuned and optimized to elevate the accuracy of ligand structures. This entailed rectifying the bond angles, mitigating the steric clashes, assigning suitable charges, and harmonizing the overall geometry of the GQD and compounds. Furthermore, meticulous attention was dedicated to ensuring compatibility with the molecular docking software by transforming GQD and compounds into a format seamlessly aligned with the intricacies of docking simulations. This meticulous formatting ensured accurate representation throughout the docking process. Through this rigorous journey of ligand preparation, our overarching objective remained steadfast, *i.e.*, to furnish refined, optimized, and impeccably formatted structures for subsequent molecular docking simulations. The significance of this meticulous procedure cannot be overstated, given that it serves as the linchpin influencing the precision and reliability of docking results, paving the way for seamless interactions with the target protein.

5.3.3. Sculpting proteins and navigating the molecular cosmos through docking simulations. In the realm of computational biology, molecular docking has emerged as a pivotal tool in drug discovery, offering invaluable insights into the intricate dance between ligands and proteins. Embarking on this journey with AutoDock,[36] our methodology unfolded by meticulously preparing the target protein and meticulously pruning irrelevant components, while assigning atom types and charges with precision. In parallel, ligands were primed in the PDBQT format, thoughtfully imbued with essential atom types and Gasteiger charges. The subsequent phase unveiled the setting up of a grid box meticulously enveloping the active site of the target protein, providing a spatial blueprint for our docking simulations. Here, we delved into the realm of genetic algorithms, optimizing parameters to sharpen the exploration process. Embracing the Lamarckian genetic algorithm, our docking simulation iteratively refined the conformations of the ligands within the active site.[37–39] Post-simulation, we delved in the treasure trove of results, meticulously sifting through poses adorned with the lowest binding energy, meticulously dissecting crucial interactions such as hydrogen bonds. Armed with powerful visualization tools, we unraveled the tapestry of complex interplays between the ligands and proteins. To fortify the fortress of methodological rigor, we subjected our predictions to the crucible of validation against experimental data, ensuring harmonious resonance with real-world observations. Iterative refinement became our guiding compass, steering us towards enhanced predictive accuracy. However, our methodology transcends the realm of individual interactions, extending its embrace to the grand theater of high-throughput screening. Here, ligands were meticulously prioritized based on their predicted binding affinities, unfurling a roadmap towards the rational design of pharmaceutical compounds. Within the AutoDock ecosystem, our journey navigated through the labyrinthine receptor proteins of bacterial strains such as *Escherichia coli* (PDB ID: 1HNJ),[40] *Bacillus subtilis* (PDB ID: 6UF6),[41] and the fungal strain *Aspergillus niger* (PDB ID: 1UKC).[42] With AutoDock as our compass, the binding sites were demarcated using rectangular grid boxes, meticulously centered on the mean atomic coordinates. Fine-tuning docking parameters became our anthem, orchestrating the delicate dance of ligand poses with meticulous consideration of multiple parameter sets.[43,44] In the crucible of our

methodology, the optimal docked conformation adorned with the lowest score was unveiled for each ligand, revealing a symphony of interactions such as hydrogen bonding and van der Waals attractions. The ligands and receptors, meticulously prepared in.pdbqt format using AutoDock Tools, set sail on a journey of docking runs, breathing life into the landscape of computational drug discovery.

5.3.4. Harnessing innovation: advancing pharmacophore modeling. In our investigation, we embarked on a comprehensive and integrated methodology that seamlessly fused structure-based and ligand-based approaches with the pioneering auto pharmacophore technique, which was first introduced by Dubey *et al.* in 2016. Our overarching goal was to meticulously pinpoint and delineate the pivotal pharmacophoric attributes inherent within the GQDs and compounds azadirachtin (5281303), beta sitosterol (222284), catechin (9064), epicatechin (72276), gallic acid (370), gedunin (12004512), mahmoodin (126566), margolone (189728), nimbin (08058), nimbolide (12313376), quercetin (5280343) and salannol (157144). To achieve this ambitious objective, we turned to the robust and sophisticated Discovery Studio auto pharmacophore generation protocol module. This automated process encompassed a diverse array of distinctive feature types, including hydrogen bond acceptor (HB_ACCEPTOR), hydrogen bond donor (HB_DONOR), hydrophobic feature (HYDROPHOBIC), negative ionizable feature (NEG_IONIZABLE), positive ionizable feature (POS_IONIZABLE), and aromatic ring (RING_ARO-MATIC). By harnessing the rich spectrum of these feature types, we generated multiple potential pharmacophore models, each meticulously crafted to encapsulate and embody the essential elements crucial for effective binding to the target enzyme. To discern the most potent pharmacophore model amidst this wealth of options, we employed a sophisticated Genetic Function Approximation (GFA) model. This cutting-edge approach allowed us to predict selectivity with remarkable accuracy. As a result, the refined pharmacophore hypothesis that emerged from our study represented a consolidated and refined representation of the interaction mechanism. This final model seamlessly integrated the critical functional groups necessary for eliciting the desired bioactivity within the confines of the target enzyme, offering comprehensive insight into the interaction mechanism of the compounds. Our methodology stands as a testament to the power of innovation and integration in advancing pharmacophore modeling, paving the way for enhanced drug discovery and development endeavors.

5.3.5. Exploring depths: unraveling molecular behavior with DFT and MESP calculations. The density functional theory (DFT) method stands as a beacon in the realm of computational chemistry, offering a versatile toolkit to dissect the intricate nuances of materials. From energetic properties to structural configurations, electrical behavior, and optical characteristics, DFT serves as a cost-effective and reliable approach, unraveling insights across various scales, from atomic and molecular levels to larger unit cells. In our investigation, the application of DFT proved instrumental in probing numerous crucial parameters related to electronic behavior, energetics, thermodynamics, and adsorption tendencies, notably focusing on

binding energy. Additionally, it aimed to decode the reactivity of pharmacological complexes through quantum molecular descriptors such as HOMO, LUMO, band gap energy, chemical hardness, softness, electronegativity, and electrophilicity. These descriptors serve as fundamental pillars in understanding the behavior and potential of compounds within pharmacological applications. To execute these computations and optimizations, we harnessed the power of the Gaussian 09 software package as our computational tool. Gaussian 09 provided a robust platform to accurately optimize the molecular structures associated with the GQDs and compounds, including azadirachtin (5281303), beta sitosterol (222284), catechin (9064), epicatechin (72276), gallic acid (370), gedunin (12004512), mahmoodin (126566), margolone (189728), nimbin (08058), nimbolide (12313376), quercetin (5280343), and salannol (157144). Employing density functional three-parameter hybrid (B3LYP) methods together with the 6-311G(d,p) basis set ensured precise insights into the molecular characteristics, fostering a comprehensive understanding of the synthesized compounds and their potential pharmacological interactions. Furthermore, molecular electrostatic potential (MESP) diagrams were generated, particularly for the salt molecule, employing the B3LYP-D3/6-311G(d,p) method. These visual representations overlay the electrostatic potential (ESP) onto electron density (ED) surfaces, showcasing a spectrum of colors ranging from deep red to deep blue. This visualization offers a rational depiction of the electrostatic properties across the surface of the salt molecule, furnishing valuable insights into its electric charge distribution. In essence, our utilization of DFT and MESP calculations unveiled a deeper understanding of molecular behavior, paving the way for informed decision-making in pharmacological research and drug discovery endeavors.

5.3.6. Navigating drug development: unveiling ADMET properties. In the realm of drug development, mitigating the risk of clinical failure is paramount, and the anticipation and comprehension of absorption, distribution, metabolism, excretion, and toxicity (ADMET) properties stand as pivotal pillars in this endeavor. Successful prediction and assessment of these properties are crucial in steering compounds away from potential pitfalls during clinical trials, thereby enhancing their prospects of evolving into promising drug candidates. In our study, we embarked on a comprehensive evaluation of the toxicological properties exhibited by two specific compounds and a ligand employing the TOPKAT module integrated within the Discovery Studio software. Our primary objective centered on unraveling the *in silico* pharmacokinetic attributes inherent within these compounds, traversing a diverse spectrum of toxicological parameters. These factors included rat oral LD50, rodent carcinogenicity, mutagenicity, and aerobic biodegradability. Going beyond mere assessments, our study extended its scope to intricate details, including the intestinal absorption of the compounds within the human system, their ability to traverse the blood–brain barrier and penetrate the central nervous system, alongside an in-depth analysis of their metabolic pathways. The evaluation was not confined to singular assessments but rather delved into multifaceted examinations to estimate the total drug clearance and toxicity levels associated with these molecules. This holistic

d on 11 2567. Downloaded on 3/2/2569 16:49:08.

This article is licensed under a Creative Commons Attribution 3.0 Unported Licence.

Paper

Materials Advances

View Article Online

Table 2 Comprehensive summary of molecular docking, DFT, MESP, and ADMET analyses for 12 bioactive compounds with graphene quantum dots

Compound	Target/analysis	Key metric without GQDs	Key metric with GQDs	Major observations/changes	ADMET properties
Azadirachtin	*E. coli* (Docking)	Binding energy: −95.21 kcal mol⁻¹	Binding energy: −124.77 kcal mol⁻¹	Enhanced hydrogen bonding (Thr81, His85)	Good GI absorption; low BBB permeability; no toxicity predicted
	DFT	Band gap: 0.116 eV	Band gap: 0.002 eV	Significant electronic interaction improvement	Optimal molar refractivity; high bioavailability
	MESP	Neutral potential	Weak negative potential	Dominated by van der Waals interactions	
Beta-sitosterol	*E. coli* (Docking)	Binding energy: −101.87 kcal mol⁻¹	Binding energy: −131.43 kcal mol⁻¹	Shifted interaction with Asp107, Asn193	Good GI absorption; poor BBB permeability; no toxicity predicted
	DFT	Band gap: 0.193 eV	Band gap: 0.001 eV	Minor electronic changes, stable polarity	Moderate water solubility, suitable for oral formulations
	MESP	Negative potential	Strong negative potential	Hydroxyl group contributes to electrostatic attraction	
Catechin	*A. niger* (Docking)	Binding energy: −81.84 kcal mol⁻¹	Binding energy: −186.29 kcal mol⁻¹	Strong H-bonding (Ser133, Thr455)	Good GI absorption; low BBB permeability; no toxicity predicted
	DFT	Band gap: 0.150 eV	Band gap: 0.002 eV	Moderate electronic interaction with GQDs	High bioavailability; strong anti-oxidant potential
	MESP	Negative potential	Enhanced negative potential	Attractive electrostatic interactions	
Epicatechin	*A. niger* (Docking)	Binding energy: −75.55 kcal mol⁻¹	Binding energy: −180.01 kcal mol⁻¹	Enhanced interactions (Ser133, Leu444)	Good GI absorption; low BBB permeability; no toxicity predicted
	DFT	Band gap: 0.141 eV	Band gap: 0.001 eV	Subtle electronic enhancements	Moderate bioavailability; anti-oxidant properties
	MESP	Negative potential	Negative potential	Attractive π–π stacking interactions	
Gallic acid	*A. niger* (Docking)	Binding energy: −60.89 kcal mol⁻¹	Binding energy: −165.35 kcal mol⁻¹	Expanded hydrogen bonding network with Thr455	High GI absorption; no BBB permeability; low skin penetration
	DFT	Band gap: 0.122 eV	Band gap: 0.001 eV	Subtle electronic modification, retains polarity	High bioavailability; no major toxicity predicted
	MESP	Negative potential	Negative potential	Strong interaction at edges of GQDs	
Gedunin	*B. subtilis* (Docking)	Binding energy: −129.05 kcal mol⁻¹	Binding energy: −293.92 kcal mol⁻¹	Enhanced steric interactions	Moderate GI absorption; no BBB permeability; low toxicity risk
	DFT	Band gap: 0.103 eV	Band gap: 0.005 eV	Reduced electronic reactivity with GQDs	Suitable for oral use; promising anticancer potential
Mahmoodin	*B. subtilis* (Docking)	Binding energy: −137.89 kcal mol⁻¹	Binding energy: −302.75 kcal mol⁻¹	Strong H-bonding with Asp146, Thr91	Good GI absorption; no BBB permeability; no toxicity predicted
	DFT	Band gap: 0.103 eV	Band gap: 0.002 eV	Improved conductivity with GQDs	Potential anti-inflammatory properties
Margolone	*A. niger* (Docking)	Binding energy: −77.17 kcal mol⁻¹	Binding energy: −181.63 kcal mol⁻¹	Enhanced steric reconfiguration	Moderate GI absorption; no BBB permeability; no toxicity predicted
	DFT	Band gap: 0.106 eV	Band gap: 0.002 eV	Subtle enhancements in electron transfer	Antimalarial activity potential
Nimbin	*E. coli* (Docking)	Binding energy: −165.95 kcal mol⁻¹	Binding energy: −330.81 kcal mol⁻¹	Significant steric interaction changes	Moderate GI absorption; no BBB permeability; low toxicity risk
	DFT	Band gap: 0.084 eV	Band gap: 0.003 eV	Increased reactivity and reduced band gap	Promising antimicrobial properties
Nimbolide	*B. subtilis* (Docking)	Binding energy: −166.47 kcal mol⁻¹	Binding energy: −331.33 kcal mol⁻¹	Notable steric reorientation with residues	Good GI absorption; moderate BBB permeability; predicted hepatotoxicity risk
	DFT	Band gap: 0.079 eV	Band gap: 0.003 eV	Increased reactivity with reduced band gap	Acceptable skin permeability; potential liver enzyme inhibition
	MESP	Neutral potential	Slightly negative potential	Polarity influenced by interaction geometry	
Quercetin	*A. niger* (Docking)	Binding energy: −78.24 kcal mol⁻¹	Binding energy: −182.69 kcal mol⁻¹	π–π stacking contributes to stability	High GI absorption; moderate BBB permeability; low toxicity risk.
	DFT	Band gap: 0.109 eV	Band gap: 0.008 eV	Enhanced conductivity due to reduced band gap	High bioavailability; suitable for oral formulations
	MESP	Negative potential	Negative potential	Strong hydrogen bonding with surface residues	
Salannol	*A. niger* (Docking)	Binding energy: −99.40 kcal mol⁻¹	Binding energy: −203.86 kcal mol⁻¹	Enhanced steric and H-bonding interactions	Moderate GI absorption; no BBB permeability; low toxicity risk
	DFT	Band gap: 0.133 eV	Band gap: 0.002 eV	Retained electronic stability	Anti-inflammatory potential

approach provided comprehensive insights into the safety profiles and pharmacokinetic behaviors of the compounds, thereby facilitating a deeper understanding of their potential efficacy and safety as drug candidates.

5.4. Statistical analysis

The experiments were performed in triplicate. The obtained results were subjected to statistical analysis using the GraphPad Prism software. The experimental data were processed by one-way analysis of variance (ANOVA) with Tukey test at a 95% confidence interval. Each value represents the mean ± SD, wherein the P value represents the level of significant changes. The XRD, UV-visible spectra, and histogram were plotted in "Origin Pro 2023".

6. Conclusions

This study demonstrated the efficient production of GQDs using plant extracts. The approach advocated here prioritizes

824 | *Mater. Adv.*, 2025, **6**, 805–826

© 2025 The Author(s). Published by the Royal Society of Chemistry

the reduction of harmful chemicals by providing an improved substitute to current industry practice for the synthesis of nanomaterials. The size, shape and morphology of the phyto-mediated GQDs were confirmed by HRTEM and SEM. The size distribution graph from TEM revealed that the particle size of GQDs was less than 10 nm. Finally, the antioxidant activity of the phyto-mediated GQDs was tested and they showed better results than the crude extract, paving the way to explore their potential applications such as bioimaging, cytotoxicity, and beyond. In conclusion, the synthesis of GQDs using compounds extracted from *Azadirachta indica* leaves demonstrated promising antioxidant, antibacterial, and antifungal activities. These findings were observed both *in vitro* and through *in silico* analyses utilizing various computational techniques such as molecular docking, pharmacophore modelling, density functional theory (DFT), and ADMET prediction. The *in vitro* experiments revealed that the synthesized GQDs + 12 compounds exhibited significant antioxidant properties, which was attributed to the presence of bioactive compounds derived from *A. indica* leaves. These antioxidant properties have the potential to combat oxidative stress-related diseases and conditions effectively. Moreover, the GQDs + 12 compounds displayed antibacterial and antifungal activities *in vitro*, suggesting their potential as novel antimicrobial agents. These activities were likely due to the interaction of GQDs + 12 compounds with the bacterial and fungal cell membranes, disrupting their integrity and leading to microbial inhibition. The computational analyses (Table 2), including molecular docking, pharmacophore modelling, DFT calculations, and ADMET prediction, provided valuable insights into the molecular interactions, energetics, and pharmacokinetic properties of the GQDs and their constituent compounds. These computational approaches supported the experimental findings and enhanced our understanding of the bioactivity mechanisms of the GQDs + 12 compounds. In summary, the combination of experimental and computational approaches highlighted the potential of *A. indica* leaf-derived GQDs + 12 compounds as versatile nanomaterials with potent antioxidant, antibacterial, and antifungal properties. The antibacterial studies further demonstrated the efficacy of GQDs, with their inhibition zones reaching up to 14.1 ± 0.2 mm against *Bacillus subtilis* at a concentration of 100 μg mL^{-1}, indicating their superior performance compared to the leaf extract. These results are consistent with the computational predictions that GQDs would enhance binding interactions with bacterial proteins, suggesting their utility in combating bacterial infections.

Future research efforts should focus on elucidating the specific underlying molecular mechanisms for their bioactivity, optimizing their synthesis and formulation for various applications.

Author contributions

Pooja Kadyan: writing – original draft (experimental), methodology, data curation, investigation characterization, validation, performed experiment. Manish Kumar: writing – review & editing (Biological work), validation, visualization, and formal analysis. Aisha Tufail: writing the original Draft (*in silico* work), visualization, validation. Andrea Ragusa: formal analysis and validation. Sudhir Kumar Kataria: supervision (Experimental), conceptualization, writing – review & editing (experimental), validation and formal analysis. Amit Dubey: supervision (computational), writing the original draft (*in silico* work and Biological work), conceptualization, software (molecular docking, DFT, MESP, pharmacophore modeling and ADMET), visualization, methodology, writing – review & editing, validation and formal analysis.

Data availability

The data supporting this article have been included as part of the ESI.†

Conflicts of interest

The authors declare no conflicts of interest.

Acknowledgements

References

1 F. Prestinaci, P. Pezzotti and A. Pantosti, *Pathog. Global Health*, 2015, **7**, 309–318.
2 T. J. Masho, P. T. Arasu, R. F. Bogale, E. AmareZerrefa and S. Ramamurthy, *Res. Chem.*, 2024, **2**, 11–101369.
3 R. B. Asamoah, E. Annan, B. Mensah, P. Nbelayim, V. Apalangya, B. Onwona-Agyeman and A. Yaya, *Adv. Mater. Sci. Eng.*, 2020, **1**, 1–8.
4 K. Habiba, D. P. Bracho-Rincon and J. A. Gonzalez-Feliciano, *et al.*, *Appl. Mater. Today*, 2015, **1**, 80–87.
5 M. A. Kohanski, D. J. Dwyer and J. J. Collins, *Nat. Rev. Microbiol.*, 2010, **8**, 423–435.
6 S. Liu, T. H. Zeng and M. Hofmann, *et al.*, *ACS Nano*, 2011, **5**, 6971–6980.
7 K. D. Patel, R. K. Singh and H. W. Kim, *Mater. Horiz.*, 2019, **6**, 434–469.
8 M. Gaur, C. Misra, A. B. Yadav, S. Swaroop, F. Ó. Maolmhuaidh, M. Bechelany and A. Barhoum, *Materials*, 2021, **14**, 5978.
9 O. Zaytseva and G. Neumann, *Chem. Biol. Technol. Agric.*, 2016, **3**, 1–26.

10 J. Deng, M. Li and Y. Wang, *Green Chem.*, 2016, **18**, 4824–4854.

11 D. Pan, J. Zhang, Z. Li and M. Wu, *Adv. Mater.*, 2010, **22**, 734–738.

12 L. Centeno, J. Romero-García, C. Alvarado-Canché and C. Gallardo-Vega, *et al.*, *Sens. Bio-Sens. Res.*, 2021, **1**, 32–100412.

13 P. Kumar, C. Dhand, N. Dwivedi and S. Singh, *et al.*, *Renewable Sustainable Energy Rev.*, 2022, **1**, 157–111993.

14 P. Kadyan, R. Malik, S. Bhatia and A. Al Harrasi, *et al.*, *J. Nanotechnol.*, 2023, **1**, 1–26.

15 C. Xiong, J. Xu, Q. Han, C. Qin, L. Dai and Y. Ni, *Cellulose*, 2021, **28**, 10359–10372.

16 L. Othman and R. M. Abdel-Massih, *Front. Microbiol.*, 2019, **10**, 453561.

17 V. Sharma, *J. Pharm. Innov.*, 2018, **7**, 648–650.

18 P. Kadyan Thillai, P. Arasu and S. K. Kataria, *Int. J. Biomater.*, 2024, **1**, 2626006.

19 W. H. Danial, M. Abdullah, M. A. A. Bakar and M. S. Yunos, *et al.*, *Opt. Mater.*, 2022, **132**, 112853.

20 R. V. Khose, G. Chakraborty, M. P. Bondarde and P. H. Wadekar, *et al.*, *New J. Chem.*, 2021, **45**, 4617–4625.

21 W. Shi, H. Fan, S. Ai and L. Zhu, *New J. Chem.*, 2015, **39**, 7054–7059.

22 Y. Yan, S. Manickam, E. Lester, T. Wu and C. H. Pang, *Ultrason. Sonochem.*, 2021, **73**, 105519.

23 S. C. Gupta, S. Prasad., A. K. Tyagi, A. B. Kunnumakkara and B. B. Aggarwal, *Phytomedicine*, 2017, **34**, 14–20.

24 S. Saleem, G. Muhammad, M. A. Hussain and S. N. Bukhari, *Phytother. Res.*, 2018, **7**, 1241.

25 M. O. Daniyan and O. T. Ojo, *J. Mol. Graphics Modell.*, 2019, **87**, 144.

26 S. Siddiqui, S. Faizi, B. S. Siddiqui and Ghiasuddin, *J. Nat. Prod.*, 1992, **55**, 303.

27 R. Murugan and T. Parimelazhagan, *J. King Saud Univ., Sci.*, 2014, **26**, 267–275.

28 M. K. Kumawat, M. Thakur, R. B. Gurung and R. Srivastava, *ACS Sustainable Chem. Eng.*, 2017, **5**, 1382–1391.

29 Y. Qiu, Y. Zhang, M. Yu, X. Li, Y. Wang, Z. Ma and S. Liu, *Small*, 2024, 2310087.

30 Z. Fang, Q. Zhou, W. Zhang and J. Wang, *et al.*, *Materials*, 2023, **16**, 7583.

31 D. Hajra and S. Paul, *Pharm. Res.*, 2018, **10**(4), 347–353.

32 M. I. Okeke, C. U. Iroegbu, E. N. Eze, A. S. Okoli and C. O. Esimone, *J. Ethnopharmacol.*, 2001, **78**, 119–127.

33 C. Tshangana, M. Chabalala, A. Muleja, E. Nxumalo and B. Mamba, *J. Env. Chem. Eng.*, 2020, **4**, 103930.

34 J. Dundas, Z. Ouyang, J. Tseng, A. Binkowski, Y. Turpaz and J. Liang, *Nucleic Acid Res.*, 2006, **1**, 116.

35 W. Tian, C. Chen, X. Lei, J. Zhao and J. Liang, *Nucleic Acids Res.*, 2018, **46**, 363–367.

36 G. M. Morris, R. Huey, W. Lindstrom, M. F. Sanner, R. K. Belew, D. S. Goodsell and A. J. Olson, *J. Comput. Chem.*, 2009, **30**, 2785–2791.

37 A. Dubey, A. Facchiano, P. W. Ramteke and A. Marabotti, *Future Med. Chem.*, 2016, **8**, 841–851.

38 A. Dubey, A. Marabotti, P. W. Ramteke and A. Facchiano, *Biochem. Biophys. Res. Commun.*, 2016, **473**, 449–454.

39 A. Dubey, M. M. Alawi, T. A. Alandijany, I. M. Alsaady, S. A. Altwaim, A. K. Sahoo, V. D. Dwivedi and E. I. Azhar, *Viruses*, 2023, **15**, 251.

40 X. Qiu, C. A. Janson, W. W. Smith, M. Head, J. Lonsdale and A. K. Konstantinidis, *J. Mol. Biol.*, 2001, **307**, 341–356.

41 F. K. Li, F. I. Rosell, R. T. Gale, J. P. Simorre, E. D. Brown and N. C. Strynadka, *J. Biol. Chem.*, 2020, **295**, 2629–2639.

42 M. V. Keniya, M. Sabherwal, R. K. Wilson and M. A. Woods, *et al.*, *Antimicrob. Agents Chemother.*, 2018, **62**, 10–1128.

43 S. Bharadwaj, A. Dubey, N. K. Kamboj, A. K. Sahoo, S. G. Kang and U. Yadava, *Sci. Rep.*, 2021, **11**, 10169.

44 A. Dubey, S. Dotolo, P. W. Ramteke, A. Facchiano and A. Marabotti, *Biomolecules*, 2018, **9**, 5.